

An Implicit Discontinuous Galerkin Method For Modeling Acute Edema and Resuscitation In The Small Intestine

Travis B. Thompson^{1,c,2,*}, Beatrice Riviere^{b,1}, Matthew Knepley^a

^aDept. of Comp. Sci. and Eng., Univ. at Buffalo, Buffalo, New York.

^bDept. of Comp. and App. Math, Rice University, Houston, TX

^cDept. of Numer. Anal. and Sci. Comp. , Simula Research Laboratory AS. Fornebu, Norway

1. Introduction

Edema refers to a generalized condition where fluid collects in the regions between cells *due to the local disruption of fluid-content balance* . Despite this simple description, edema development and propagation dynamics can rely on several factors; as noted in a comprehensive review paper [82] these include venous and lymphatic pressure and flow, serum protein concentrations and alterations in microvascular permeability. A useful clinical model for understanding the emergence of edema is found in fluid-balance equations; one such equation, known as the Starling-Landis-Drake-Laine model, is given in condensed form by:

$$\frac{dV}{dt} = J_V - J_L, \quad (1.1)$$

where V represents the fluid volume of a tissue compartment, J_V encapsulates factors regarding the microvascular fluid exchange and J_L models lymphatic flow. Edema can result when, for example, J_V is sufficiently larger than J_L for extended periods of time. The terms J_V and J_L each rely on extended constituents such as the venous / lymphatic pressure and serum protein concentrations mentioned above; section 3.1.2 contains a more detailed discussion of these terms.

Edema, resulting from an imbalance in (1.1), can arise alongside various clinical pathologies, in different organs, and may complicate treatment; examples include cirrhosis, hydrocephalus, and acute respiratory distress syndrome, among others [55, 58, 65, 93]. Edema in the small intestine can be triggered by

*Corresponding Author

Email addresses: `tthompson@simula.no` (Travis B. Thompson), `riviere@caam.rice.edu` (Beatrice Riviere)

¹Supported in part by NSF-DMS 1312391

²Research conducted partially at Dept of Comp and App Math, Rice University, Houston, TX. Supported in part by NSF-DMS 1312391

traumatic injury in addition to clinical processes, such as packing a wound, or surgical treatment [23]. Edema in the small bowel can stiffen tissue fibers, and increase the distance between synapses responsible for contractile function [38]; a severe reduction in motility, referred to as ileus, can result. *Ileus is an occlusion (mechanical ileus) or paralysis (functional ileus) of the bowel preventing the forward passage of the intestinal contents, causing their accumulation proximal to the site of the blockage [92]. Ileus is a common clinical condition and can prolong recovery times or result in fatality [23, 29, 64] for extreme cases.*

Edema dynamics have been modeled in several ways. Black-box models are often used in the medical literature; these models reduce complex physiology, such as tissue networks, extracellular matrices and chemical reactions, to a system of tanks with directional exchanges representing homogenization of the tissue fluid dynamics [29, 27, 28, 73, 84]. Black-box type models [29, 27] typically employ ordinary differential equations, such as (1.1), directly to describe fluid exchange in terms of *their related averaged parameters* fitted by means of clinical experiment [20, 73]. *While careful black-box type approaches may be beneficial for estimating underlying parameters in particular regimes of clinical interest they, however, neglect the coupled fluid-mechanical response of the tissue.* Clinical edema models for predictive use could benefit from the inclusion of mechanical response. As fluid seeps into the interstitial area between cells, the extracellular tissue matrix may expand. Fluid-tissue interaction can induce secondary effects leading to symptomatic expression; including ileus in the intestine or increased intracranial pressure in hydrocephalus [55, 64]. In-silico numerical models coupling the mechanical response, and fluid balance have often employed the framework of poroelasticity theory [21, 63, 86, 87, 91]. This framework was introduced first by Terzaghi [85], developed further by Biot [12, 13, 14, 15], and generalized to multiple fluid networks by Barenblatt [8], and Aifantis [2, 11, 45, 97].

In this *manuscript*, Biot's theory of linear poroelasticity is used to explore the evolution of severe edema in the small intestine. *A primary motivation of the work is to test a recent clinical [23] hypothesis regarding the efficacy of utilizing a 7.5% hypertonic saline solution to abet the effects of severe edema.* The numerical approach for the model is predicated on a recent work *utilizing a novel mixed formulation of the linear, quasi-static poroelasticity equations [77]. The equations* are discretized with the discontinuous Galerkin (DG) method. DG methods are widely used in mechanics for their local mass conservation properties [77]; their ability to handle solution and parameter discontinuities make them a natural choice for the layered physiology of the intestine. The implicit Euler method is used to discretize the time derivative. The proposed approach in this manuscript offers several novel advantages, and additional clinical insights, over a previous work [99]. The early model used an explicit time-stepping scheme, ignored the intrinsic storage coefficient of the tissue, and was strictly two-dimensional. The proposed method is implicit in time, allows for a non-zero intrinsic storage coefficient, is more robust with regard to spurious pressure oscillations, and has been shown to converge [77]. The proposed model includes a novel accounting for the phenomenon of Starling overestimation in

the context of high venous pressures.

From a numerical point of view the implicit in time discretization yields increased stability in time [17, 24, 61] and allows for larger time steps. The numerical technique utilized in the proposed approach *utilizes* the non-symmetric interior penalty (NIPG) method with dual penalty parameters. *This choice was made based on the author’s previous results [77] demonstrating that the non-symmetric (NIPG) formulation was more robust to the presence of non-physical pressure oscillations; such oscillations are referred to as poroelastic locking. Though the symmetric (SIPG) and non-symmetric (NIPG) DG methods, on simplicial meshes, have been shown to be locking-free [42, 95] when solving the equations of linear elasticity such non-physical oscillations can still arise for Biot’s equations when storage coefficients and hydraulic conductivities are low; this parameter regime arises in soft-tissue biomechanical applications. In a previous paper [77] we endeavored a locking-behavior comparison of the NIPG and SIPG method variants; there, we demonstrated computationally that the dual-penalty NIPG approach can decrease the severity of possible spurious oscillations by several orders of magnitude over the corresponding SIPG discretization. In addition we observed that spurious pressure oscillations, for both NIPG and SIPG, were removed entirely when using higher order polynomial spaces for the discretization of the displacement; as has been suggested by others [70]. Recent stabilization techniques [78] discretizing the Biot system, with improved monotonicity properties, could also be considered for addressing any spurious pressure oscillations. In our previous investigation an a priori analysis for the numerical discretization, presented herein, was also conducted [77].*

From a clinical point of view, *our incorporation* of the intrinsic storage coefficient *into the improved model* is not only more accurate, physiologically, but produces new insight into the effects of acute edema and hypertonic saline resuscitation with regard to intestinal motility. Moreover, the results in this manuscript are discussed strictly in the context of three-dimensional computations performed on a physiologically-to-scale mesh with luminal features. Finally, the model incorporates a correction for the Starling overestimation [43, 51] phenomena thought to occur due to micro-scale stretching of the vascular endothelium when venous pressure is high.

The remainder of the paper is organized as follows: Section 2 offers a brief clinical motivation for the work and overviews the supporting results; Section 3 covers the fundamentals of modeling edema in the intestine; including basic macro-physiology, interstitial fluid balance, and the equations of linear poroelasticity. Section 3.4 discusses an extension of our previously introduced numerical scheme [77] for use in the intestinal model. Section 4 discusses the clinical experiment [23] in detail and results of the computational simulations relating directly to the measured quantities of that experiment. Section 5 contains additional results related to the clinical experiment; these results may not be observable by clinicians in a laboratory setting and highlight the advantage of enhancing clinical inquiry via computational modeling. Concluding remarks are given in Section 6.

2. A Clinical Motivation

Clinical experiments can be limited by several factors including cost, ethical approval, and constraints making extended measurements difficult. One advantage of a computational model is the ability to test paradigms that may be difficult in a laboratory setting or to garner insight into results that were unmeasured, or immeasurable, in the original clinical study. This section briefly discusses several results of the paper which pertain to exploring a clinical question of interest. As mentioned in Section 1 a recent clinical experiment [23] postulates that 7.5% hypertonic saline solution may be an effective resuscitation fluid to mitigate the early-onset effects of severe intestinal edema. The clinicians postulate that 7.5% hypertonic saline resuscitation could lead to a reduction of hydrostatic pressure in the submucosa and a subsequent, possibly partial, restoration of contractile function and motility due to lower applied volume-induced stress on the muscle layer from the submucosal layer.

Basic intestinal physiology and a computational model of edema formation is first discussed in section 3. This model has the potential for wider application in exploring questions related to edema formation in the intestine. As a first focus we consider the model applied to investigate 7.5% hypertonic saline modulation of the intestinal pressure and fluid balance; the topic of the aforementioned experiment [23]. The connection between the clinical experiment and the numerical model is primarily embodied by four parameters: K_f , P_V , Π_V , and P_p . These quantities are first explained in section 3.1.2, and a comprehensive parameter discussion is endeavored in section 3.3. Parameters with respect to normal conditions were taken directly, or estimated, from the literature. However, it is necessary to use experimentally specific values, or adjustments, for some of these parameters.

The clinical experiment of interest [23] consisted of four different groups of male Sprague-Dawley rats; each group was comprised of six animals. The four groups, and their differences, are described at length in section 4.1; two of the experiments, the control (CTRL) and hypertonic saline (HS) cases, established baseline effects and two experiments, the elevated venous pressure (EVP) and elevated venous pressure with hypertonic saline (EVP-HS), taken together test the efficacy of 7.5% hypertonic saline solution resuscitation. Section 4.2 discusses the influence of the experiment on the four main model parameters (K_f , P_V , Π_V , and P_p) and what parameters were calibrated using the CTRL and HS baseline experiments.

Section 4.1 discusses the primary quantity, submucosal pressure, measured by clinical researchers in the course of the experimental procedure; in addition, for one experiment, tissue water content was also measured. Clinicians accorded [23] a drop in submucosal pressure, following 7.5% hypertonic saline injection in the presence of elevated venous pressure, as corresponding to reduced intestinal tissue stress and an increase in contractile, and motile, capacity. Our model supports their observation that high submucosal pressures, following the induction of acute edema, are reduced post-hypertonic saline injection; suggesting that 7.5% hypertonic saline may indeed be an effective resuscitation agent for miti-

gating edema. A comprehensive discussion of the primary computational results, *i.e.* those that can be directly assessed against the reported clinical experimental observations, is presented in section 4.4.

A further advantage of computational models is the ability to gain insight into aspects that may not have been investigated in the laboratory experiment. In this regard our model offers additional results that also corroborate the conclusion that 7.5% hypertonic saline can act to modulate the effects of acute edema formation. These results are contained in section 5. In particular section 5.1 suggests that the interstitial pressures should decrease in all intestinal layers following application of 7.5% hypertonic saline. Moreover, following resuscitation, relative pressures should be lowest in the mucosal layer (see figure 7) and the model also predicts that luminal attenuation will decrease dramatically (see figure 8). These observations may act to increase overall intestinal motility; especially if contractile function in the muscle layers is, at least partially, restored as discussed in the next paragraph. Such effects were not quantified, or were possibly too difficult to investigate in tandem, in the clinical experimental report of [23].

Finally, section 5.2 advances a novel argument in corroboration with the clinical hypothesis of 7.5% hypertonic saline effectiveness by utilizing the computational model's water content predictions (see section 5.1) to infer a subsequent impact of resuscitation on contractile function. The model results suggest that 7.5% hypertonic saline may act to restore the signaling capacity of enteric neurons by reducing average diffusion distances, following the onset of severe edema, and thus promote an increase in contractile function. The computational model described in this manuscript is not only in agreement with the primary clinical findings but offers additional and novel support to the clinical conclusion that 7.5% hypertonic saline resuscitation could restore intestinal function following edema. These results are suggestive that follow-up clinical experiments may be warranted.

3. A Poroelastic Model of Interstitial Edema in the Intestine

This section describes the framework of the mathematical model for edema formation in the intestine. Section 3.1 contains a brief overview of the macro-scale intestinal physiology necessary for the conceptualization of the model in addition to the medical equations of fluid balance; 3.2 describes the quasi-static Biot equations of poroelasticity; and 3.3 details the parameters used in the model.

3.1. Macro-Physiology and Interstitial Fluid Balance

An overview of basic intestinal physiology [36, 41, 44, 98] is given in 3.1.1, and clinical models of vascular-tissue fluid exchange are discussed in 3.1.2.

3.1.1. An Introduction to the Macro-Physiology of the Small Intestine

In this section, a succinct account of the macro-physiology of the small intestine is described. We note that the small intestine is an intricate, and fascinating, multi-scale structure embodying both macro-scale and micro-scale features expressing biological function. The purpose of this section is to provide an overview of the macro-level features which play a role in the computational modeling considerations; namely the different layers of the small bowel, as their distinct mechanical moduli play a role in the current work. We do not attempt to give a full account of the intestinal physiology at all scales; for this, the interested reader is referred to comprehensive medical texts [36, 39, 41].

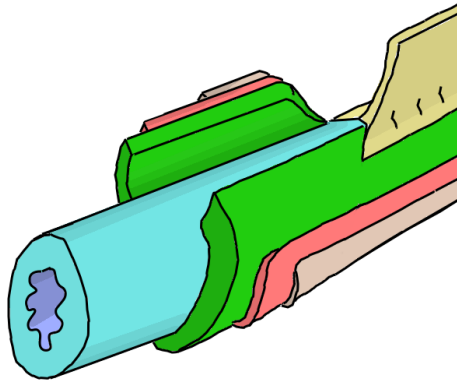


Figure 1: Resected Cross Sectional Macro-Physiology of the Small Bowel. Purple: Lumen, Blue: Mucosa Green: Submucosa, Pink: Muscularis Externa, Tan: Serosa and Gold: Mesentery Attachment

The small intestine is a tube-like structure, and part of the gastrointestinal tract. The small intestine connects the stomach at the duodenum, proceeds to the jejunum, and terminates distally at the ileum where it is separated by the cecum of the large intestine by the ileocecal valve. The macro-physiology of the small intestine that we will describe here, shown in Figure 1, is: a luminal cavity, four tissue layers, and the mesentery attachment. *The distinct layers in figure 1 have been resected and non-anatomically shaded*

to improve illustrative visibility .

Each intestinal layer is physiologically distinct [36]; *these layers form a tube-like structure enveloping a central lumen, or inner void space, through which content passes (shaded purple in figure 1) . Moving radially outward from the lumen is the mucosal layer (shaded blue), submucosa (shaded green), muscularis externa (shaded pink), and finally the serosa (shaded tan). The mesentery (shaded in gold) attaches the small intestine to the abdominal wall, and supplies nerve fibers, blood, and lymphatic vessels. These structures are juxtaposed, in a cut-away format, together in figure 1. The mucosa accounts for sixty to eighty percent of the intestinal wall thickness, and is primarily responsible for the absorption of nutrients. The submucosa makes up ten to fifteen percent of the radial thickness, and is made up of elastic fibrils, and connective tissue. The muscularis externa and serosa form a ‘muscle layer’ which lubricates and protects the intestinal tissue. The muscle layer also produces peristaltic contractions; such contractions assist in the procession of luminal content [36, 41, 44]. We consider the muscularis externa and serosa as a combined ‘muscle layer’ due to their thinness, and similar mechanical properties. Each layer of the intestine is permeated by blood capillaries, and lymphatic vessels; however, vessel density*

is higher in the mucosal, and submucosal layers [39, 62]. *Though the capillaries and lymphatic vessels are not depicted in figure 1, accounting for their role in the model is the topic of section 3.1.2. Further micro-structures, such as the epithelium lining the lumen, the villi and the microvillus protruding into the lumen from the mucosal wall, the thin muscularis mucosae bordering the mucosal and submucosal layers, etc are not considered in the present work; details regarding these structures can be found in medical texts [36, 39, 41].*

3.1.2. Fluid Balance In the Interstitium

Parameter	Description
K_F	microvascular filtration coefficient
P_V	microvascular hydrostatic pressure
σ	protein permeability of blood capillaries ($\sigma \in [0, 1]$)
Π_V	microvascular oncotic pressure
Π_I	interstitial oncotic pressure
R_L	effective lymphatic resistance
P_P	lymph pumping pressure
P_L	hydrostatic pressure of lymph capillaries

Table 1: Terms of the Starling-Landis and Drake-Laine equations

The interstitium, or intercellular region, contains an interstitial fluid phase, and the structural molecules of the extracellular matrix [96]. *Capillaries move fluid into the interstitium, while both capillaries and lymphatics participate in the outflow of fluid from the interstitium [79];* the exchange is regulated by hydrostatic and oncotic pressure gradients. Mathematical models aimed at explaining the fluid balance in the interstitium relate microvascular filtration, mostly responsible for fluid inflow, and lymphatic return which largely regulates fluid outflow; the difference reflects interstitial fluid storage.

$$J_V(p) = K_F (P_V - p - \sigma(\Pi_V - \Pi_I)) \quad (3.1)$$

$$J_L(p) = R_L^{-1} (p + P_P - P_L) \quad (3.2)$$

Fluid balance has been studied for use in various organs such as the lung [93, 94], and brain [67, 73, 87]. The most popular model of microvascular filtration is the Starling-Landis [48, 67, 69] equation, J_V , and the Drake-Laine equation, J_L , models lymph flow [29]. The Starling-Landis-Drake-Laine (SLDL) approach has been used for generalized interstitial spaces [29, 27]. The SLDL model employs (3.1)-(3.2) to model the balance of interstitial fluid volume, V , as $\frac{\partial V}{\partial t} = J_V(p) - J_L(p)$. This produces a linear function of the *interstitial* pressure, p . The terms of (3.1)-(3.2) are described in *table 1*. Common fluid balance modeling in the medical literature is done by solving the ODE $\frac{\partial V}{\partial t} = J_V - J_L$ as part of a compartmental system approach; the focus is typically that of a ‘black box’ with parameter-fitting and neglects the mechanical response of the tissue

[29, 27, 28, 84]. Incorporating this response is a primary goal of the present work.

$$\Phi(\mathbf{x}, p(\mathbf{x}, t)) = \frac{\eta}{V_0} C(\mathbf{x}) (J_V(p(\mathbf{x}, t)) - J_L(p(\mathbf{x}, t))) \quad (3.3)$$

In this work the fluid model is given by (3.3) with J_V , and J_L given by (3.1)-(3.2). The additional quantities in (3.3) are: V_0 is a fixed reference volume that facilitates the compatibility of units with the equations of poroelasticity described in section 3.2; $C(\mathbf{x}) \in (0, 1]$ is a dimensionless, spatial capillary distribution function where \mathbf{x} is a point in the intestinal domain; $\eta > 0$ is a dimensionless scaling factor. The term $\frac{\eta}{V_0} C(\mathbf{x})$ can be interpreted as a fitted capillary density for the fluid model. An adaptation to (3.3) for the term (3.1) in the presence of high microvascular pressure and local oncotic pressure differences will be discussed in 4.2.

3.2. The Quasi-Static Biot Equations Of Linear Poroelasticity

Modeling biological tissues via the quasi-static Biot equation [4, 9, 83] is an increasingly popular choice in biomechanics; recent models have also incorporated more than one tissue-fluid network [86, 91, 90]. The organ is assumed a linearly poroelastic medium consisting of an isotropic (tissue) solid skeleton permeated by a single-phase fluid. Deformations are assumed small, and inertial forces are neglected. An overview of the derivation of Biot's equations, and generalizations to multiple fluid networks, can be found in e.g. [4, 9, 83]. The displacement formulation of the linear, quasi-static Biot equations for an isotropic poroelastic medium, used in this work, is given by:

$$\frac{\partial}{\partial t} (c_1 p + c_0 \nabla \cdot \mathbf{w}) - \kappa \Delta p = \Phi(p) \quad \text{in } \Omega \times [0, T], \quad (3.4)$$

$$-\mu \Delta \mathbf{w} + c_0 \nabla p - (\mu + \lambda) \nabla (\nabla \cdot \mathbf{w}) = 0 \quad \text{in } \Omega \times [0, T], \quad (3.5)$$

In (3.4)-(3.5) \mathbf{w} denotes the displacement of the solid (tissue) skeleton and p is the hydraulic (interstitial) pore pressure; $\Phi(p)$ is a (pressure-dependent) source function. Conservation of mass is expressed in (3.4), and (3.5) reflects conservation of momentum. The shear modulus of the tissue is μ , and λ is related to the tissue's Young's modulus. The hydraulic conductivity is denoted with κ , c_0 is the Biot-Willis constant and c_1 is the storage coefficient. Further detail of physical significance of the material parameters can be found in [4, 60].

3.3. A Model Of Edema In the Intestine

This section details value selection for the physical parameters, and fluid balance model (3.3), applicable for the small intestine. The parameters utilized in our model are summarized in Table 2. *Parameters with citations (table 2) were garnered from the clinical literature values via a survey conducted for our previous work [99]. Parameter values, in table 2 marked with an asterisk were obtained via calibration for the specific cases listed; these include the reflection*

Starling-Landis Model				
Parameter	Selected Value	Units	Description	References
K_f	121.0	ml/(mmHg·h)	Low pres.	[20, 40]
	160.0	ml/(mmHg·h)	High pres.	[20, 40]
P_V	12.0	mmHg	Normal	[23, 39]
	20.0	mmHg	EVP case	[23]
σ	0.8	-	Normal K_f	[20, 36, 40]
	0.45	-	High K_f	*
Π_V	18.5	mmHg	CTRL case	*
	20.0		Normal	[18, 74]
Π_I	12.0	mmHg	-	[40, 75]
Drake-Laine Model				
Parameter	Selected Avg. Value	Units	Designation	References
R_L^{-1}	43.1	ml/(mmHg·h)	-	[40]
P_p	12.0	mmHg	Low pres.	[28, 39, 88]
	28.0		High pres.	[28, 39, 88]
P_L	2.0	mmHg	-	[28]
Reference Interstitial Space				
V_0	8400	ml	Ref. volume	[20]
p_{thr}	2.3	mmHg	Threshold pres.	[36, 38]

Table 2: SLDL Fluid Balance Model Parameters

* Parameter determined via model calibration

coefficient, σ , in the case of high capillary filtration (K_f) and the microvascular oncotic pressure (Π_V ; change from baseline due to surgical trauma). The estimation of these two values, for these specific cases, is discussed in section 4.2

The abbreviations CTRL and EVP refer to clinical experiments discussed in Section 4. For the capillary distribution function, $C(\mathbf{x})$ in (3.3), a piecewise linear model is used. This choice proved most effective in exploratory work [98]. $C(\mathbf{x})$ obtains a maximum value $C(\mathbf{x}_{\text{muc}}) = 1$ on the interface of the mucosa-lumen boundary, and decreases linearly in the mucosa to the submucosa. In the submucosa the value is $C(\mathbf{x}_{\text{submuc}}) = 0.001$, and in the musculature the value is $C(\mathbf{x}_{\text{musc}}) = 0.002$. This reflects the relative distribution of capillaries within the intestinal structure [36]; Figure 2 shows a graph of the distribution superimposed on a test mesh. To specify the poroelasticity model for the intestine some adaptations are necessary. The internal physiology of the intestine is layered (see Fig 1). Each layer is characterized by its own set of (μ, λ) parameters [23]. Within each layer the isotropic, quasi-static, linearly poroelastic assumptions are assumed to hold.

$$\mu(p), \lambda(p) = \begin{cases} \mu_1, \lambda_1 & p < p_{thr} \\ \mu_2, \lambda_2 & p \geq p_{thr} \end{cases} \quad (3.6)$$

Clinical experiments have shown that the values of μ , and λ in the intestine

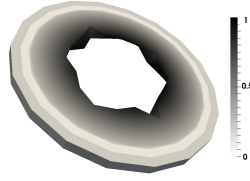
$p < p_{thr}$				$p \geq p_{thr}$		
	Mucosa	Submucosa	Muscle	Mucosa	Submucosa	Muscle
μ (mmHg)	3	1050	120	1.5	750	60
λ (mmHg)	7.5	2625	300	3.75	1875	150

Table 3: Lamé parameters (in mmHg)

Biot-Willis (c_0)	Storage (c_1 , mucosa)	Hydraulic Conductivity (κ)
0.99	$4.5 \times 10^{-10} \text{ Pa}^{-1}$	$4.540 \times 10^{-13} \text{ m}^2/\text{Pa} \cdot \text{s}$

Table 4: Coefficients in Biot's model

are pressure dependent [36, 38, 71], i.e. $\mu = \mu(p)$ and $\lambda = \lambda(p)$. *This effect could be due to local connective tissue degradation at high pressure. More specifically, clinical experiments [23, 71] investigated changes to μ and λ in the presence of edema by performing stretch and opening angle [41, 89] measurements on tissues in various stages of induced edema. It was shown [71] that as the venous pressure increased, i.e. increased severity of induced edema, differences in the specimen elastic properties were observed. In [23] high venous pressures were correlated to elevated interstitial pressure; further establishing the suggestive relation $\mu = \mu(p)$ and $\lambda = \lambda(p)$. In our earlier work [98, 99] the pressure-dependent changes to μ and λ were established in collaboration with the authors of the original clinical study [23] based on their laboratory measurements.* It is assumed that the pressure dependence is piecewise constant, and based on a threshold pressure, p_{thr} as in (3.6). Pressure-dependent values [22, 23, 36, 38, 71] of μ and λ are shown in table 3. The scaling relation $c_1 \approx \lambda^{-1}$ has also been assumed [50, 60] and is incorporated into the model via: $p > p_{thr}$ implies $c_1 \rightarrow c_1(\lambda_1/\lambda_2)$.

Figure 2: $C(\mathbf{x}) \in (0, 1]$. Higher values are darker

For pressure exceeding p_{thr} the shift in (μ, λ, c_1) reflects the damaged state of the respective intestinal layer. *For this simplified damage model [23, 71] the values of μ , and λ are changed within a layer once the average pressure of that layer exceeds p_{thr} . Localized damage models, based on clinical studies of soft-*

tissue injury under high pressures, may further refine results.

The remaining model values to be specified are: the hydraulic conductivity κ , Biot-Willis coefficient c_0 , and storage coefficient c_1 ; see table 4. The hydraulic conductivity is assumed uniform, and estimated from studies conducted on whole bovine trachea [31]; the physiology of the trachea is layered, and similar to the intestine. A common assumption in soil models [4], also reasonable for soft tissues [26], is that the Biot-Willis coefficient is $c_0 \approx 1$. Following [90] we select $c_0 = 0.99$, and $c_1 = 4.5 \times 10^{-10} \text{ Pa}^{-1}$. Due to the transition of

tissue composition between the mucosa, and muscle layer we estimate c_1 in the submucosa as one order of magnitude lower, and two orders of magnitude lower in the muscle layer.

3.4. An Implicit Discontinuous Galerkin Discretization

In this section we discuss an extension to a previously proposed [77] implicit in time discontinuous Galerkin discretization for a mixed formulation of (3.4)-(3.5) for use with clinical simulations of intestinal edema. Section 3.4.1 describes the mixed formulation of (3.4)-(3.5) and section 3.4.2 details the extension of the discrete scheme presented found in [77]. Early models for intestinal edema have used an explicit-in-time discretization [99] which relies on the assumption that the constrained storage coefficient is zero. Not only is this assumption physiologically inaccurate in the intestine, but explicit in time discretizations can affect the stability condition of the method resulting in a restrictive time step size [17, 24, 61]. Early investigation [17] of a Lagrange finite element discretization of Biot's equation examined the θ family of one-step time-discretization methods given by:

$$y^{n+1} - y^n \approx \Delta t (\theta f(t^n, y^n) + (1 - \theta)f(t^{n+1}, y^{n+1})).$$

It was shown that the resulting time-space discretization was unconditionally stable for $\theta \leq \frac{1}{2}$. For $\theta > \frac{1}{2}$ a restrictive stability requirement was needed. A Von-Neumann stability analysis [61] later showed that for fully saturated porous media, explicit schemes ($\theta = 1$) are infeasible for general use, and controlling spurious oscillations in the pore pressure requires a fully implicit ($\theta = 0$) time integration scheme.

3.4.1. A Mixed Formulation of Biot's Equations and Boundary Conditions

Define the dilatation $\epsilon = \nabla \cdot \mathbf{w}$ extending equations (3.4)-(3.5) and consider the following mixed form of Biot's equations:

$$-\mu \Delta \mathbf{w} + c_0 \nabla p - (\mu + \lambda) \nabla \epsilon = 0, \quad \text{in } \Omega \times [0, T], \quad (3.7)$$

$$\nabla \cdot \mathbf{w} - \epsilon = 0, \quad \text{in } \Omega \times [0, T], \quad (3.8)$$

$$c_1 \frac{\partial p}{\partial t} + c_0 \frac{\partial \epsilon}{\partial t} - \kappa \Delta p = \Phi(p), \quad \text{in } \Omega \times [0, T]. \quad (3.9)$$

$\Omega \subset \mathbb{R}^d$ is assumed to be a bounded, convex domain, with smooth boundary $\partial\Omega$. The boundary is decomposed into disjoint Dirichlet and Neumann sections, for the displacement and pressure, by $\partial\Omega = \Gamma_{wD} \cup \Gamma_{wN}$ and $\partial\Omega = \Gamma_{pD} \cup \Gamma_{pN}$ where $\Gamma_{wD} \cap \Gamma_{wN} = \Gamma_{pD} \cap \Gamma_{pN} = \emptyset$.

$$\begin{aligned} p &= p_D && \text{on } \Gamma_{pD} \times (0, T) \\ \kappa \nabla p \cdot \mathbf{n} &= g_p && \text{on } \Gamma_{pN} \times (0, T) \\ \mathbf{w} &= \mathbf{w}_D && \text{on } \Gamma_{wD} \times (0, T) \\ \mu \nabla \mathbf{w} \cdot \mathbf{n} + (\mu + \lambda) \epsilon \mathbf{n} - c_0 p \mathbf{n} &= g_W && \text{on } \Gamma_{wN} \times (0, T) \end{aligned} \quad (3.10)$$

The boundary conditions considered for the model are (3.10). Pressure is prescribed on Γ_{pD} , and displacement on Γ_{wD} , while on Γ_{pN} a Darcy flux is imposed. On Γ_{wN} the displacement formulation of the Cauchy normal stress condition, $\sigma \cdot \mathbf{n} = g_W$ where σ is the Cauchy stress tensor, is enforced. In our application, $g_W = 0$ is used on Γ_{wN} , $g_p = 0$ on Γ_{pN} and the boundary measure of the set Γ_{pD} is zero. More details on the boundary locations for the intestinal geometry will be discussed in section 4.3.

3.4.2. Discretization and An Extension To the Intestinal Model

The (intestinal) domain Ω is triangulated with a quasi-uniform [76] tetrahedral mesh \mathbf{T}_h with maximum element diameter denoted h . Equations (3.7) - (3.9) are then discretized in space via the discontinuous Galerkin (DG) method [76]. The discretization follows the procedure in [77], with a slight extension; the purpose of this section is to briefly describe the extension to the bilinear forms appearing in the previous work and refer the interested reader there for more details.

The discretization of the mixed equations (3.7)-(3.9) is carried out in [77] under the assumption of constant lame parameters μ , and λ . As discussed in section 3.3 clinical experiments show that μ and λ take on different values in each layer of the intestine, and are pressure dependent [36, 38, 71]. In the present work it is assumed that the Lamé parameters satisfy a piecewise constant dependence on the pressure; see e.g. *table 3*, (3.6), and the value of p_{thr} in *table 2*. Towards this let $\tilde{\mu}(p)$, and $\tilde{\lambda}(p)$ denote element-wise constant approximations to the pressure-dependent parameters $\mu(p)$, and $\lambda(p)$. In this manuscript $\tilde{\mu}(p)$ and $\tilde{\lambda}(p)$ are defined by evaluating the numerical pressure at the barycenter of each element and using (3.6). Let $M_h \times M_h \times \mathbf{V}_h$ be the discrete DG spaces defined as in [77]. Then the extended discrete scheme (compare to e.g. equations (10)-(11) in [77]) can be stated as follows:

Given $(p_h^n, \varepsilon_h^n, \mathbf{w}_h^n)$ in $M_h \times M_h \times \mathbf{V}_h$, find $(p_h^{n+1}, \varepsilon_h^{n+1}, \mathbf{w}_h^{n+1})$ in $M_h \times M_h \times \mathbf{V}_h$ such that for every $(r, q, \mathbf{v}) \in (M_h \times M_h \times \mathbf{V}_h)$ we have

$$\begin{aligned} & c_1 \left(\frac{p_h^{n+1} - p_h^n}{\Delta t}, r \right)_\Omega + c_0 \left(\frac{\varepsilon_h^{n+1} - \varepsilon_h^n}{\Delta t}, r \right)_\Omega + \kappa a_1(p_h^{n+1}, r) \\ & = (\Phi(p_h^n), r)_\Omega + \ell_1(t^{n+1}; r), \quad \forall n \geq 0, \end{aligned} \quad (3.11)$$

$$(\varepsilon_h^{n+1}, q)_\Omega + b(\mathbf{w}_h^{n+1}, q) = \ell_2(t^{n+1}; q), \quad \forall n \geq -1, \quad (3.12)$$

$$\begin{aligned} & a_{2,\mu}(\mathbf{w}_h^{n+1}, \mathbf{v}) + j \left(\frac{\mathbf{w}_h^{n+1} - \mathbf{w}_h^n}{\Delta t}, \mathbf{v} \right) - b_{\mu+\lambda}(\mathbf{v}, \varepsilon_h^{n+1}) + c_0 b(\mathbf{v}, p_h^{n+1}) \\ & = \ell_3(t^{n+1}; \mathbf{v}) + \sum_{e \in \Gamma_{wD}} \frac{\sigma_2}{h_e} \left(\frac{\mathbf{w}_D(t^{n+1}) - \mathbf{w}_D(t^n)}{\Delta t}, \mathbf{v} \right)_e, \quad \forall n \geq 0, \end{aligned} \quad (3.13)$$

The only modifications in (3.11)-(3.13) to those of the previous work (equations (10)-(11) in [77]) are those made to the bilinear forms of equations (3.12)-(3.13). These have been altered by:

$$\begin{aligned}
a_{2,\mu}(\mathbf{w}, \mathbf{v}) &= \sum_{E \in \mathcal{T}_h} (\tilde{\mu}(p) \nabla \mathbf{w}, \nabla \mathbf{v})_E - \sum_{e \in \Gamma_h \cup \Gamma_{wD}} (\{\tilde{\mu}(p) \nabla \mathbf{w}\} \cdot \mathbf{n}_e, [\mathbf{v}])_e \\
&+ \theta_2 \sum_{e \in \Gamma_h \cup \Gamma_{wD}} (\{\tilde{\mu}(p) \nabla \mathbf{v}\} \cdot \mathbf{n}_e, [\mathbf{w}])_e + \sum_{e \in \Gamma_h \cup \Gamma_{wD}} \frac{\sigma_2}{h_e} \{\tilde{\mu}(p)\} ([\mathbf{w}], [\mathbf{v}])_e, \quad (3.14)
\end{aligned}$$

$$b_{\mu+\lambda}(\mathbf{v}, q) = - \sum_{E \in \mathcal{T}_h} (\nabla \cdot \mathbf{v}, q)_E + \sum_{e \in \Gamma_h \cup \Gamma_{wD}} (\{\tilde{\mu}(p) + \tilde{\lambda}(p)\} q, [\mathbf{v}] \cdot \mathbf{n}_e)_e, \quad (3.15)$$

More specifically, in [77] the Lamé parameters μ and λ were assumed constant throughout the medium. In accordance with the damage model discussed in section 3.3 the pressure-dependent Lamé parameters still assume constant values within a layer. Thus, within the same layer, equations (3.14)-(3.15) simplify to those previously analyzed [77] and are given by:

$$\begin{aligned}
a_{2,\mu}(\mathbf{w}, \mathbf{v}) &= \sum_{E \in \mathcal{T}_h} \tilde{\mu}(\nabla \mathbf{w}, \nabla \mathbf{v})_E - \sum_{e \in \Gamma_h \cup \Gamma_{wD}} \tilde{\mu}(\nabla \mathbf{w} \cdot \mathbf{n}_e, [\mathbf{v}])_e \\
&+ \theta_2 \sum_{e \in \Gamma_h \cup \Gamma_{wD}} \tilde{\mu}(\nabla \mathbf{v} \cdot \mathbf{n}_e, [\mathbf{w}])_e + \sum_{e \in \Gamma_h \cup \Gamma_{wD}} \frac{\sigma_2}{h_e} \tilde{\mu}([\mathbf{w}], [\mathbf{v}])_e,
\end{aligned}$$

$$b_{\mu+\lambda}(\mathbf{v}, q) = - \sum_{E \in \mathcal{T}_h} (\nabla \cdot \mathbf{v}, q)_E + \sum_{e \in \Gamma_h \cup \Gamma_{wD}} (\tilde{\mu} + \tilde{\lambda}) (\{q\}, [\mathbf{v}] \cdot \mathbf{n}_e)_e,$$

The scheme used in the biomedical computations for the intestine, is therefore given by (3.11) - (3.15) where $\Phi(p^n)$, in (3.11), is defined by (3.3). In practice, we take $\theta_1 = \theta_2 = 1$ (appearing in the bilinear forms $a_1(p_h, q_h)$ and $a_{2,\mu}(\mathbf{w}_h, \mathbf{v}_h)$) as the non-symmetric (NIPG) variant of the scheme was shown to be more robust to non-physical pressure oscillations often seen in discretizations of Biot's equations [77]. The penalty value used for σ_2 , in (3.14), is 1×10^1 while the penalty value used for σ_1 , analogously defined in the bilinear form $a_1(p_h, r)$ of (3.11), is 1×10^{-2} .

3.4.3. Summary of Numerical Method A Priori Behavior

The simulations described in section 4 utilize the numerical method given by (3.11)-(3.15); to facilitate computational cost considerations the discrete spaces, M_h (pressure and dilatation) and V_h (displacement), were chosen to consist of element-wise linear DG functions. When the Lamé parameters agree on both elements of a common edge, such as within the same intestinal layer, equations (3.14)-(3.15) reduce to a discrete scheme for constant Lamé parameters studied by the authors in a previous work [77]. In [77] we endeavored an extensive a priori convergence analysis for both the non-symmetric (NIPG) and symmetric (SIPG) variants of the approach. In this section we briefly recall our a priori

convergence result for the NIPG discretization and refer the interested reader to [77] for a full discussion and formal proof. Assume that the Lamé coefficients are constant throughout the domain, as is the case within each intestinal layer, then in [77] we have proven the following result for the NIPG method:

THEOREM 3.1 (The non-symmetric interior penalty (NIPG) method) Assume that $\Delta t < 1$, $c_1 > 0$ and that $\theta_2 = 1$ in (3.14) so that the form $a_{2,\mu}$ is non-symmetric. Let k_m denote the polynomial degree of the DG space M_h , k_v the polynomial degree of the DG space V_h , and L_Φ the Lipschitz continuity constant of the source function Φ . Then there exists a constant C independent of h , Δt , as well as c_0, κ, λ such that for any $m \geq 1$:

$$\begin{aligned} c_1 \|p^m - p_h^m\|_{L^2(\Omega)}^2 &\leq Ch^{2k_m} c_1 \|p^m\|_{H^{k_m+1}(\Omega)}^2 + \mathcal{B}, \\ (\mu + \lambda) \|\epsilon^m - \epsilon_h^m\|_{L^2(\Omega)}^2 &\leq C(\mu + \lambda) h^{2k_m} \|\epsilon^m\|_{H^{k_m+1}(\Omega)}^2 + \mathcal{B}, \\ \Delta t \kappa \sum_{n=1}^m \|p^n - p_h^n\|_M^2 &\leq \kappa Ch^{2k_m} \|p\|_{L^\infty(0,T;H^{k_m+1}(\Omega))}^2 + \mathcal{B}, \\ \mu \|\mathbf{w}^m - \mathbf{w}_h^m\|_V^2 &\leq \mu Ch^{2k_v} \|\mathbf{w}^m\|_{H^{k_v+1}(\Omega)}^2 + \mathcal{B}, \end{aligned}$$

where the quantity \mathcal{B} is defined as:

$$\mathcal{B} = C(\mu, c_1, T)(\mathcal{A} + C\mu h^{2k_v} \|\mathbf{w}\|_{L^\infty(0,T;H^{k_v+1}(\Omega))}^2),$$

and \mathcal{A} is defined by:

$$\begin{aligned} \mathcal{A} &= C(c_1, T) \left(\left(\frac{L_\Phi^2}{\kappa} + c_0^2 + \kappa \right) h^{2k_m} \|p\|_{L^\infty(0,T;H^{k_m+1}(\Omega))}^2 \right. \\ &\quad + h^{2k_m+2} (\mu + \lambda)^2 \|\epsilon\|_{L^\infty(0,T;H^{k_m+1}(\Omega))}^2 + \left(1 + \frac{c_0^2}{\kappa} + (\mu + \lambda) \right) h^{2k_v} \|\mathbf{w}_t\|_{L^\infty(0,T;H^{k_v+1}(\Omega))}^2 \\ &\quad + (\mu + \lambda) Ch^{2k_v} \|\mathbf{w}_0\|_{H^{k_v+1}(\Omega)}^2 + \frac{\Delta t^2}{\kappa} (c_1^2 \|p_{tt}\|_{L^\infty(0,T;L^2(\Omega))}^2 \\ &\quad \left. + c_0^2 \|\epsilon_{tt}\|_{L^\infty(0,T;L^2(\Omega))}^2 + L_\Phi^2 \|p_t\|_{L^\infty(0,T;L^2(\Omega))}^2) \right). \end{aligned}$$

In particular, the a priori analysis predicts optimal convergence rates for the dilatation, pressure, and displacement in the L^2 , M and V norms, respectively; here, the M and V norm notation represents the standard DG energy norm [76] on the corresponding spaces. Optimal L^2 convergence rates for the pressure and displacement errors were observed computationally [77]. Moreover, an implication of the above is that the best overall convergence rates are achieved when $k_m = k_v$; that is, when the DG spaces M_h and V_h are chosen to be of the same polynomial degree. We close this section by re-iterating that several additional results, such as the symmetric (SIPG) scheme and when the storage coefficient, c_1 , vanishes are discussed in our previous work [77]. In addition, the interested reader will find that a numerical study of spurious pressure oscillations has been conducted and that the predicted convergence rates have been verified, in both time and space, using the method of manufactured solutions.

Abbrev.	Description
CTRL	Sham surgical procedure
EVP	Large infusion of normal saline, and a suture to induce elevated venous pressure
HS	An infusion of hypertonic saline
EVP-HS	A large infusion of normal saline, a suture to induce elevated venous pressure, an infusion of hypertonic saline midway

Table 5: Clinical Experiments of [23]

4. Numerical Simulations Of A Clinical Experiment

The suitability of the computational model for clinical *applications* is tested via comparison to a published medical experiment [23] from the Center for Microvascular and Lymphatic Studies, at the University of Texas-Houston Medical School, in conjunction with the DeBakey Institute at Texas A&M University. Section 4.1 is an overview of the clinical experiment while section 4.2 relates the experiment and the mathematical model; section 4.3 covers details of the numerical implementation; section 4.4 discusses results of the direct computational analogs carried out in the clinical experiment. Section 4.1 overviews the clinical study [23] of interest and section 4.2 discusses the link between the constituent clinical experiments and the mathematical model.

4.1. Experimental Procedure

The overall focus of a recent clinical study [23] was to investigate whether acute edema may impair the contractile function of the intestine, and to judge the effects of 7.5% hypertonic saline resuscitation in abetting acute edema expression. The effects of intestinal edema were investigated via four clinical experiments on male Sprague-Dawley rats: a control case (CTRL), a 7.5% hypertonic-saline infusion (HS), an Elevated venous pressure case (EVP), and an elevated venous pressure followed by 7.5% hypertonic saline administration (EVP-HS). Each group was anesthetized 12-16 hours before surgical procedure, and fasted. A silastic catheter was placed into the main intestinal lymphatic vessel, the superior mesenteric vein was dissected free of its mesenteric attachment, and a pressure transducer catheter was inserted into the submucosal layer of the small intestine.

The four treatments are as follows: the CTRL group received a sham (placebo) surgical procedure. The EVP group was given a large infusion of normal saline, and a suture of the mesenteric vein to induce elevated venous pressure EVP. The HS group received a small infusion hypertonic saline HS. The EVP-HS group was given a large infusion of normal saline, suturing of the mesenteric vein, and halfway through the experiment a small infusion hypertonic saline. Submucosal pressure measurements were taken at thirty minutes after preparation. In addition to the submucosal pressure measurements, the interstitial fluid volume

Clinical Ranges of Experimental Parameters		
Parameter	Range	References
P_V	10.0-12.0 mmHg	[23, 39]
Π_V	20.0-25.9 mmHg	[40, 75]
K_f	121-200 (ml/mmHg·h)	[20, 40]
P_p	10.0-30.0 mmHg	[28, 39, 88]

Table 6: Normal Clinical Parameter Ranges

gain was also estimated for the EVP case via a wet-dry ratio measurement process. Table 5 provides a quick reference to the experimental abbreviations, and descriptions.

4.2. Experimental Relationship to the Mathematical Model

Modeling the clinical experiment relies primarily on the modulation of four parameter values from (3.3): K_f , P_V , Π_V , and P_p . Normal clinical ranges for these values are shown in table 6. The CTRL case was used to calibrate a baseline oncotic blood pressure Π_V . Following a surgical procedure Π_V can be slightly lower than normal in-vivo values due to incurred trauma [16, 35, 56, 68]. Likewise, capillary physiology can change substantially in the presence of elevated venous pressure exceeding 15 mmHg [81]; the EVP case was therefore used to calibrate the $K_f - \sigma$ change relationship; more detail is given below. Variation of the parameters in the clinical experiment were as follows: In the CTRL and HS case a value of 12 mmHg was used for P_V . In the EVP and EVP-HS cases the suturing procedure produced P_V measured in the ranges of 17 mmHg - 23 mmHg; the median value of 20 mmHg was used in the EVP and EVP-HS computations. For the CTRL and HS cases, a baseline value of $P_p = 15$ mmHg was used. The lymphatic system is known to respond to higher venous pressure with increased lymph flow [39], and so in the case of EVP and EVP-HS, a value of 28 mmHg was used for P_p .

For the cases CTRL, and HS the normal baseline value for K_f of 121 ml/mmHg was used. In the case of EVP, and EVP-HS the suture-induced high values of P_V cause a stretching of the endothelial layer of the vessels; this raises the value of K_f and lowers the value of σ , the reflection coefficient in (3.3), commensurately [81]; this dynamic has been observed experimentally [57]. A value of $K_f = 160$ mmHg was used in the EVP and EVP-HS cases, the EVP case was then used to find a compatible value of σ . Computations were matched to the clinically reported average submucosal pressure for the EVP case yielding a value of $\sigma = 0.45$; this value is also used for the EVP-HS case before the administration of hypertonic saline. The baseline normal [33] physiological value of $\sigma = 0.8$ was used in both the CTRL and HS cases as K_f was taken in the normal physiological range.

The oncotic blood pressure, Π_V , is altered primarily in two ways relevant to the experimental tests. First, a drop in oncotic blood pressure due to surgical preparation procedures can occur for various reasons; including blood loss, or

Numerical Values for Clinical Experiments					
Experiment	P_V	Π_V	K_f	P_p	σ
CTRL	12	18.5	121	15	0.8
HS	12	20	121	15	0.8
EVP	20	18.5	160	28	0.45
EVP-HS	20	18.5 / 20	160 / 121	28	0.45 / 0.8

Table 7: Representative Experimental Model Parameters

the trauma of the surgery itself [16, 35, 56, 68]. The CTRL case computations were matched to clinical experimental average results by altering only Π_V , to gauge surgical impact to baseline oncotic pressure. This resulted in a slight decrease in Π_V , below normal homeostatic conditions, to 18.5 mmHg. This value was used in the CTRL and EVP experiments. Secondly, when vascular oncotic pressure, Π_V , is low administration of hypertonic saline is known to expand local plasma volume, increasing Π_V to near-normal levels [32, 46, 59], though this resuscitation effect can wane after several hours due to blood-protein washdown effects. The experimental time-window, at thirty minutes, is not long enough to warrant inclusion of protein-washdown effects in the model; thus, we take $\Pi_V = 20$ mmHg, the normal value, in the cases of HS and EVP-HS post-injection of hypertonic saline. Finally, an increase in Π_V coincides with a decreases in K_f [39]; thus, in the EVP-HS post-injection case K_f is returned to the baseline value of $K_f = 121$ ml/mmHg and σ is returned to the normal value of $\sigma = 0.8$ to reflect the resuscitation effect of hypertonic saline.

$$\Phi(\mathbf{x}, p(\mathbf{x}, t)) = \frac{\eta}{V_0} C(\mathbf{x}) (\mathcal{J}_V(p(\mathbf{x}, t)) - J_L(p(\mathbf{x}, t))) \quad (4.1)$$

The parameter quantities discussed for use in the experimental simulation are given summarized in *table 7*. The EVP-HS experiment is characterized by values separated by a slash to demarcate the pre-injection (left) values from the post-injection (right) values for the hypertonic saline administered at the half-way mark of the procedure. We close this section with a mention of a correctional modification to the fluid balance equation (3.3) for the EVP-HS case. Recent experiments [43, 51] have observed that the Starling equation over-estimates the vascular filtration rate in the case of high P_V , exceeding 15 mmHg, and the introduction of local oncotic pressure gradients such as via albumin perfusates. Hypertonic saline injection expands local plasma volume, raising Π_V locally on one side of the endothelium, and the model takes this into account by using a corrected Starling equation that takes the form $\mathcal{J}_V = (1/M)J_V$; see (3.3) versus (4.1). A correction factor can be estimated from experimental clinical data [43] on Starling-overestimation in this context. The correction factor $M = 2.75$ is used in the model for the EVP-HS case post hypertonic saline injection; for all other cases, including EVP-HS pre-injection of hypertonic saline, $M = 1$ and $\mathcal{J}_V = J_V$ as expected.

4.3. Implementation of the Numerical Scheme

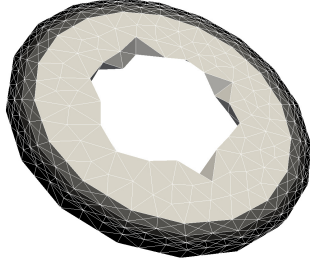


Figure 3: Thin slice of a rat small intestine

ear system. Preconditioning schemes for Biot type problems are an ongoing field of research [50]; to avoid any issues with experimental comparison, from e.g. preconditioning or iterative solver choice, SuperLU [54, 52, 53] was used to facilitate a direct solve via LU factorization. The small bowel of a Sprague-Dawley rat has an approximate radius of $r = 0.18$ cm [37]; to-scale meshes were created using Gmsh [34]. Figure 3 shows a view of a single slice of the basic geometry; the mucosa being the lightest inner layer, then the submucosa (gray), and the combined musculature (black) layers of the muscularis externa, and the serosa. The first 3D section is defined in the x-y plane, and further layers are then stacked in the +Z direction. The Lamé parameters being a constant value within each layer of the intestine is enforced in the model through the use of the average pressure. After each time step the layer average pressure is computed from the previous pressure solution; if the layer's average pressure exceeds the threshold value p_{thr} , see *table 2*, the layer's Lamé parameters are modified via (3.6) and *table 3*. The change in tissue Lamé parameters is speculated to be caused by a breakdown in connective tissues due to the high pressure load. Once a tissue layer has been damaged it remains in the damaged state for the duration of the simulation.

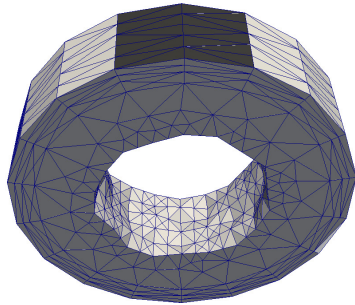


Figure 4: mesentery Boundary faces

The non-symmetric (NIPG) variant of (3.11)-(3.13) is used to carry out the computations; in a previous work [77] this approach was more robust in alleviating possible spurious oscillations in the numerical pressure when used with differing values of σ_1 , and σ_2 . As discussed, $\sigma_1 = 1 \times 10^{-2}$, and $\sigma_2 = 1 \times 10^1$ for the simulations in this manuscript. The scheme (3.11) - (3.15) was implemented using the C programming language, using PETSc [7, 5, 6] to assemble and solve the lin-

Let $\Gamma = \partial\Omega$ denote the boundary of the computational domain, Ω . For the pressure we take the Neumann boundary to be $\Gamma_{pN} = \Gamma$ and $g_p = 0$. From a physical perspective this means that the interstitial fluid cannot penetrate the boundary. For the displacement a homogeneous Dirichlet boundary condition, $\mathbf{w} = 0$, is symmetrically imposed on the top of the intestinal mesh for the faces constituting $\approx 10\%$ of the radial surface area; physiologically, this reflects the anchoring of the intestine by the mesentery; see Figure 4 where mesentery boundary faces are indicated in black.

Average Submucosal Pressures					
Experiment	6 min	12 min	18 min	24 min	30 min
CTRL	34.3	63.1	86.2	104.8	119.5
EVP	241.3	231.3	335.3	426.4	505.7
HS	13.4	24.6	33.7	41.0	46.7
EVP-HS	241.3	231.3	265.2	206.2	149.5

Table 8: Average Computed Submucosal Pressures (Pa).
Model calibration cases are shown in bold.

The condition $\mathbf{w} = 0$ is also imposed on the outermost faces, those with outward normal in the $+Z$ or $-Z$ axis direction. On all remaining faces the zero stress condition, of (3.10), is imposed; condition (3.10) is equivalent to $\sigma \cdot \mathbf{n} = 0$ where σ is the usual total stress tensor [83] of Biot's equations; physiologically, this implies that these faces are free to deform.

REMARK 4.1 The Dirichlet condition $\mathbf{w} = 0$ imposed on the end-cap face, those with outward facing normal in the $+Z$ or $-Z$ direction, reduces the capacity for tetrahedra in the outer layers to deform. It was found that using at a mesh consisting of at least five layers provides an acceptable balance, in practice, between computational complexity and capacity for layer deformation to closely approximate clinical results.

For the numerical tests, linear discontinuous Galerkin approximations were used for the displacement, dilatation, and pressure approximations. Meshes consisting of five layers balanced computational efficiency, with clinical results. All clinical quantities reported in tables 2, 4, and 6 were converted to standard units of Pascals, for pressure, milliliters, for volume, seconds, for time, and meters for length; all meshes were constructed at the physical scale of an intestine for a fully matured male Sprague Dawley rat.

4.4. Primary Computational Results

In this section the primary results of the computational experiments, e.g. those that can be most directly assessed against a corresponding clinical experiment [23], are discussed. Each of the computational experiments will be covered, beginning with the primary calibration cases; these are the control (CTRL) and elevated venous pressure (EVP) cases. As mentioned in section 4.1 the primary clinical point of comparison [23] are the submucosal pressure measurements derived, therein, from a pressure transducer reading. For comparison with this reading an average pressure within an intestinal layer, Ω_L , was computed using the canonical average value

$$p_{\text{ave},L} = \frac{1}{|\Omega_L|} \int_{\Omega_L} p \, dx. \quad (4.2)$$

The domain Ω_L could be the mucosa, submucosa, or musculature; although only measurements for the submucosa were available for comparison with experi-

Experiment	6 min	12 min	18 min
CTRL*	33.6 - 37.6	62.3 - 65.8	85.5 - 88.5
EVP*	240.5 - 264.1	227.1 - 254.4	330.9 - 355.6
HS	13.1 - 14.7	24.4 - 25.7	33.4 - 34.6
EVP-HS	237.3 - 264.8	227.4 - 254.7	253.7 - 267.5
Experiment	24 min	30 min	
CTRL*	104.2 - 106.7	119.2 - 121.2	
EVP*	422.1 - 444.5	501.7 - 522.0	
HS	40.7 - 41.7	46.6 - 47.4	
EVP-HS	193.6 - 207.9	137.8 - 151.0	

Table 9: Computed Pressure Ranges by Experiment.
Min Pressure - Max Pressure (Pa). * Model calibration cases

ment. For each computational experiment this section details: any pertinent calibrated values; final average submucosal pressure; overall minimum-maximum pressure ranges; and local-in-time minimum-maximum pressure ranges. A summary of the relevant pressure values for the section can be found in tables 8 and 9. One distinct advantage of developing, and utilizing, computational models of intestinal edema is the ability to explore additional features of the clinical experiment in a manner unencumbered by practical clinical problems such as e.g. difficulties in transducer placement within a particular intestinal layer. Towards this end, further analysis of the computational results, including observations, predictions, and suggested clinical experiments, will be covered in section 5.

4.4.1. The Control (CTRL) Computation

As discussed in 4.2 various factors, such as trauma or blood loss, encountered during surgical procedures can alter the oncotic blood pressure [16, 35, 56, 68]. The CTRL experimental case was used to ascertain a baseline oncotic blood pressure, Π_V , to be used as the reference value for the remainder of the experiments. During the calibration, all other fluid balance model parameters coincided with those found under normal conditions; only Π_V was altered. The value of $\Pi_V = 18.5$ mmHg (2466 Pa) was selected, via calibration, yielding a final computed average submucosal pressure of 119.5 Pa; this is in good agreement with the observed experimental average of ≈ 117.3 Pa [23].

The overall pressure range for the control experiment was $[0, 121]$ Pa. Corresponding min-max pressure ranges are located in the corresponding entry of table of *table 9* at five time points during the experiment; it is observed that the range of pressures varies by less than 4 Pa. The slightly reduced oncotic blood pressure (Π_V), possibly due to surgical trauma, can lead to the development of edema; though this edema should be minimal. It is not surprising then that a very slight decrease in luminal radius was observed in the course of the CTRL computational experiment; this observation is discussed in section section 5.

4.4.2. The Elevated Venous Pressure (EVP) Computation

The EVP simulation is the second fundamental calibration case; as discussed in 4.2 as the capillary filtration, K_f , raises due to increased venous pressure the reflection coefficient, σ , decreases due stretching of the endothelial layer. A value of $K_f = 160$ was selected [99] and the EVP case was utilized, at the median value of $P_V = 20 \text{ mmHg}$ (2666 Pa), to calibrate σ . The value $\sigma = 0.45$ produced a computed average submucosal pressure of 505.7; this is in good agreement with the observed experimental average of ≈ 506 Pa [23].

The final pressure range for the EVP computational experiment was approximately four times higher than that of the CTRL case at $[0, 522]$ Pa. The corresponding min-max pressure ranges at five time points, c.f. *table 9*, display a local-in-time pressure variation between 21 and 27 Pa. A distinctive reduction in luminal radius was noted during the EVP simulation due to the significant interstitial fluid volume gain; especially in the mucosa where the capillary density is highest. This facet of the computational experiment is discussed further in section 5.

4.4.3. The Hypertonic Saline (HS) Computation

The HS case was run predicatively; that is, no parameters pertinent to the model were estimated using this computational test case. As discussed in section 4.1 the HS clinical experiment was conducted by injecting a bolus of 7.5% hypertonic saline solution immediately following the conclusion of the surgical preparation procedure. An injection of hypertonic saline, a plasma volume expander [30] used in clinical fluid resuscitation, has been shown to maintain normal oncotic blood pressures in the thirty-minute time range [46] in clinical edema experiments on sheep.

The HS experiment therefore utilized a normal oncotic blood pressure value of $\Pi_V = 20 \text{ mmHg}$ (2666 Pa) [18, 74] to reflect the resuscitating effect of hypertonic saline treatment. The final average submucosal pressure for the computation was 46.7 Pa which is well within the reported experimental range [23] of 21 Pa - 112 Pa and reasonably close to the experimental average of 66 Pa. Pressure ranges at five time points suggest an local-in-time pressure variation between 1 and 2 Pa (c.f. *table 9*). Since surgical trauma can result in a slightly reduced oncotic blood pressure, one observation that we expect to see in the HS computational experiment is a reduction, or complete reversal, of luminal radius reduction. This effect was indeed observed, and is discussed in section 5.

4.4.4. The Elevated Venous Pres. - Hyp. Saline (EVP-HS) Computation

The EVP-HS case was also run predicatively; that is, no parameters were specifically calibrated with respect to this computational test case. The mean elevated blood pressure value of $P_V = 20 \text{ mmHg}$ (2666 Pa) was utilized. As discussed in section 4.1 this experiment was carried out by inducing elevated venous pressure, via the suturing procedure, followed by a bolus injection of 7.5% hypertonic saline at the midpoint of the experimental duration. The final average submucosal pressure for the computation was 149.5 Pa, and is within

the reported experimental range [23] of 99 Pa - 168 Pa and relatively close to the experimental average of 133 Pa.

A primary hypothesis of the corresponding clinical experiment [23] is that hypertonic saline may be an effective resuscitation agent in reducing, or alleviating, the onset of acute clinical edema, and that such a reduction may at least partially restore normal intestinal function. Therefore, a hypothesized outcome of the EVP-HS computational experiment is a reversal of the luminal dilatation observed in the EVP case, and some quantifiable mechanism by which intestinal motility may be restored. In this regard, the EVP-HS computational experiment did indeed verify the clinical hypothesis; further details on this observation, and additional features of the EVP-HS computational case, are discussed in section 5.

5. Discussion

In section 4.4 numerical results that could be, more or less, directly compared to the clinical experiment were discussed; in this regard the proposed model fares well as the average submucosal pressures provided by the model were reasonable approximations to those observed clinically. Section 5.1 presents computational results whose observation was limited, or unavailable, in the clinical setting. Section 5.2 discusses a method for inferring the impact of 7.5% hypertonic-saline resuscitation on intestinal motility based on the computational results. Section 5.3 elucidates clarifications to the computational model, and offers suggestions for further clinical study based on the results.

5.1. Additional Computational Results

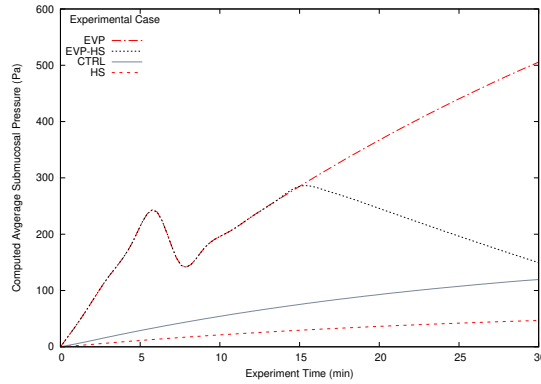


Figure 5: Average Submucosal Pressure (Pa) vs Time (min)
All Computational Experiments

The first extended result, most related to the clinical experimental measurements, is the submucosal average pressure throughout the duration of the experiment; recall that the average submucosal pressure is computed by (4.2). Figure 5 shows the average submucosal pressure (Pa) versus experimental time (min). The drop in pressure for the EVP and EVP-HS cases, occurring at approximately six minutes,

coincides with the average submucosal pressure exceeding the threshold value, p_{thr} (c.f. table 2), defining the damage model. The damage to the fibers in the

interstitium relaxes the elastic properties of the extracellular matrix, and the pressure drop here is due to the increased expansion capacity of the interstitium; the CTRL, and HS cases do not reach the threshold pressure value necessary to activate the damage model, and thus do not exhibit this feature.

It is evident from figure 5 that only the EVP and EVP-HS experiments reach the pressure threshold required to activate the damage model; this is commensurate with the experimental assumptions that the suturing procedure, coupled with a bolus injection of isotonic saline solution, induces acute edema. From figure 5 it is also observed that the HS computational case corrects for the slightly higher average pressure profile seen in the CTRL case as, possibly, a result of the surgically induced trauma leading to a slight drop in Π_V . Moreover, the primary clinical hypothesis that administration of 7.5% hypertonic saline solution may be an effective resuscitation fluid for reversing acute edema is observed; comparing the EVP curve to the EVP-HS curve a steady decline in the interstitial pressure can be seen, beginning at approximately at the 15 minute mark, coincident with hypertonic saline injection. The interstitial pressure for the EVP-HS case nearly approximates that that of the CTRL case by the end of the computation; this is consistent with laboratory results.

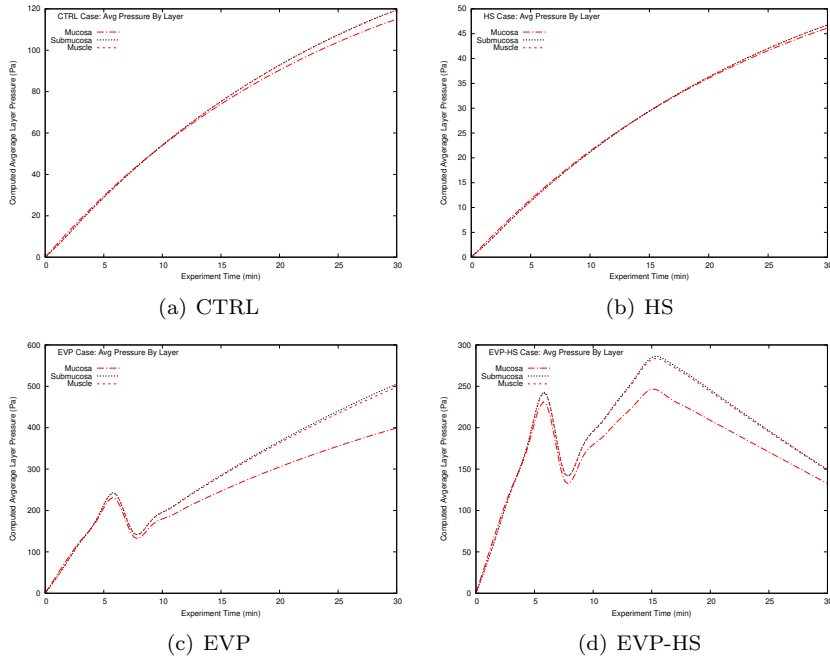


Figure 6: Average Layer Pressure (Pa) vs Time (min)
All Computational Experiments

Another closely related aspect of the computational model to clinical experiment is the average pressure in the individual layers of the intestine; in the

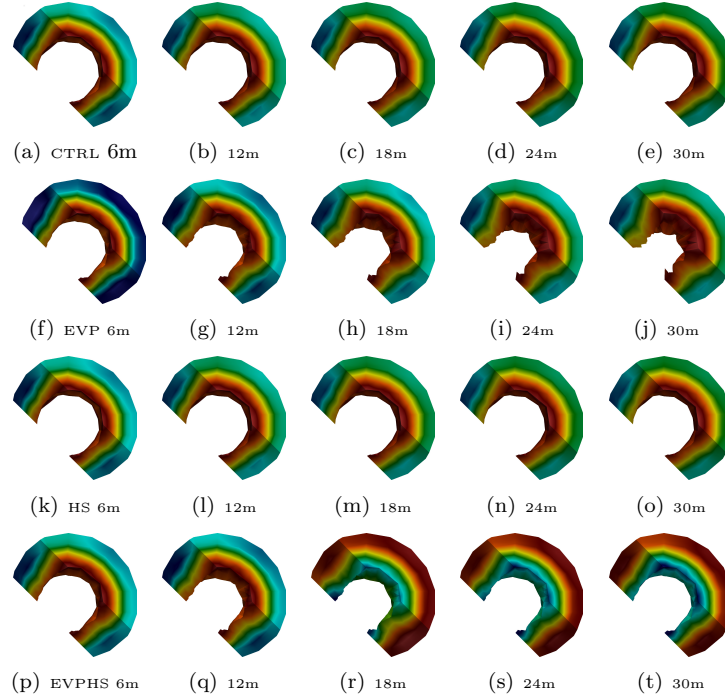


Figure 7: Intestinal Hydrostatic Pressure (Pa) Distribution, All Simulations

Coloring is with respect to the corresponding relative ranges in table 9.

Blue is the lowest relative value; warmer values are higher; red is the maximal relative value.

experimental procedure, only the submucosal pressure values were measured. Figures 6(a)-6(d) show the computational model predictions for each layer of the intestine over the duration of the clinical experiment. Consistent with the findings of a previous model [99] we see that the average layer pressure is highest in the submucosa and musculature across all experiments. For the CTRL and HS cases, figures 6(a)-6(b), the average pressures are nearly identical in every layer of the intestine. Conversely, at the conclusion of the experiment, the EVP case (figure 6(c)) displays an interlayer mucosal pressure difference of approximately 100 Pa, and for the EVP-HS case (figure 6(d)) approximately 10 Pa.

However the improved model predicts, contrary to the early model [99], that the absolute maximum pressure often occurs in the mucosa near the lumen where the capillary concentration is the highest; see figure 7 where the intestinal geometry has been sliced to allow for a comprehensive view of the pressure distribution throughout each layer. Moreover, it is clearly seen that the effects of the hypertonic saline injection manifest most prominently in the mucosa for the EVP-HS case; c.f. figures 7(p)-7(t).

The difference in the average versus maximal pressure distribution can be

explained simply by the fact that the mucosa occupies a significantly larger area, and that the maximal pressures typically occur in a localized mucosal region near the lumen; in addition, for the EVP and EVP-HS cases, the mucosa undergoes large changes in volume. This difference was not observed with the simpler, explicit model [99] which predicted minimal pressure profiles in the mucosal region and may be due to the lack of capability of the previous model to take into account the constrained storage coefficient of the tissue and its related effects.

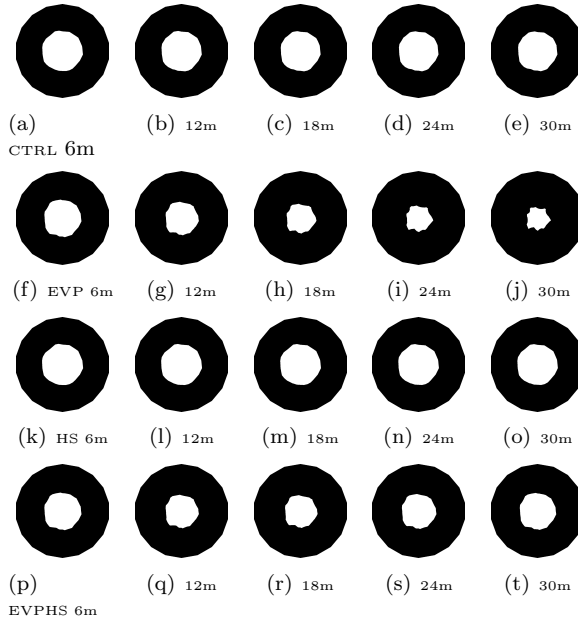


Figure 8: Lumen Radius dilatation, All Simulations

luminal volume attenuation. This is consistent with the clinical observation that edema can significantly reduce the capacity for intra-luminal transport of *content* through the intestine [23, 65, 66, 72].

The computational model also predicts a slight decrease in the lumen radius for the CTRL case (figures 8(a)-8(e)) which is consistent with the lower-than-normal oncotic blood pressure, Π_V , found in the calibration process. The latter fact, as previously mentioned, is consistent with the clinical observation [16, 35, 56, 68] that Π_V can decrease slightly as a result of the trauma associated with surgical preparation, and procedure. Comparing the CTRL case (figures 8(a)-8(e)) with the HS case (figures 8(k)-8(o)) it is observable that the slight decrease in lumen radius of the former case is abetted in the latter case; this points to the effectiveness of hypertonic saline as a resuscitative medium in the context of routine surgical practice.

Finally, and most prominently, the effects of hypertonic saline in restoring

In addition to the relative distribution of pressures, the proposed improved model of intestinal edema formation allows for the comparison of luminal radius dilatation across the various experimental regimes. Figure 8 shows an over-head view of intestinal geometry; color has been suppressed to facilitate a direct comparison of the computational predictions for the radius of the lumen across the various experimental cases. It is immediately apparent that the EVP test case (figures 8(f)-8(j)) yields a prediction of significant

Relative Volume Gain (%)					
Experiment	6 min	12 min	18 min	24 min	30 min
CTRL	0.8	1.5	2.0	2.4	2.8
HS	0.3	0.6	0.8	1.0	1.1
EVP	5.5	9.9	13.4	16.0	18.0
EVP-HS	5.5	9.9	10.9	8.7	6.5

Table 10: Final Fluid Volume Relative to Initial State.
 $P_V = 20$ mmHg for EVP and EVP-HS

luminal volume in the case of acute edema formation is clear when comparing the EVP case (figures 8(f)-8(t)) to the EVP-HS case (figures 8(p)-8(t)). Not only does the administration of hypertonic saline, occurring at the 15 min mark, reverse the initial luminal attenuation induced by the initial bolus of isotonic saline (e.g. the initial EVP experimental setup) but the final EVP-HS luminal radius (figure 8(t)) is a close approximation to the final luminal radius of the CTRL case (figure 8(e)). This resuscitation effect was a primary hypothesis of the clinical study [23] motivating the model development, and is clearly observed in the comparison of the respective sub-figures of figure 8.

We close this section with a mention of relative volume gain predicted by the computational experiment. In the clinical case [23] a selection of the intestinal tissue was harvested post-experiment from the EVP, and CTRL experimental cases; the tissue was weighed, subsequently allowed to dry, and weighed once more. Comparing these values allowed for an assessment in the relative fluid volume gain for the EVP case [99] with a mean value of 19.8%. Computationally, the relative volume gain was estimated by comparing the initial volume of the mesh to the final, deformed volume; these results are reported in *table 10*. The computed relative volume gain is predictive in the sense that the parameter calibration, mentioned for the CTRL and EVP cases, did not take into account relative volume gain for any parameter choices; only the average submucosal pressure, closely related to the clinically measured value, was utilized in the calibration process.

The computational model predicts an 18% relative volume gain for the EVP case (*table 10*, EVP case) at mean P_V ; this is a relatively reasonable approximation to the clinical measurement of a mean volume gain of 19.8%. *Table 10* shows that the computational model also predicts less volume gain for the HS experiment versus the CTRL experiment which is consistent with the luminal radius observations seen in the corresponding sub-figures of figure 8. Moreover, *table 10* offers additional quantification of the resuscitation effects of the 7.5% hypertonic saline injection (e.g. the EVP-HS case). Comparing the EVP, EVP-HS, and CTRL cases of *table 10* the computational model predicts an approximate three-fold decrease in luminal volume in the presence of acute edema formation (EVP v.s. EVP-HS) and a two-fold increase in volume over the baseline control (EVP-HS v.s. CTRL).

5.2. Estimating the impact of 7.5% hypertonic saline resuscitation contractile capacity

In this section we posit an additional argument in support of the clinical hypothesis that 7.5% saline resuscitation could mitigate the early-onset effects of severe intestinal edema; specifically, we explore the impacts of resuscitation on improving motile function of the intestine through partially restoring contractile capacity. In the clinical study [23] this inference supporting improved contractile function following hypertonic saline administration was made based on observations regarding reduced volume-induced internal stress on the muscle and mucosal layers. Here, we discuss an alternative argument in support of this hypothesis using the computational model predictions for bulk volume gain to infer a possible impact on changes in an average diffusion distance, for ions signaling contraction, due to interstitial enlargement.

Note that the current model, and the previous simplified model [99], do not contain explicit terms accounting for ion diffusion directly; as noted in review, coupling an explicit ion diffusion model with the edema framework would further strengthen predictions. Nevertheless, the current model is capable of inferring that a distinct change in average ion diffusion length, in the acute-edema (EVP) versus resuscitated edema (EVP-HS) case, is strongly plausible. To establish this conclusion we combine computational results from section 5.1 and a formula discussed in section 5.2.1 to estimate, and infer, the possible effects. In our previous work [99] a similar argument was made for an early model which does not incorporate the intrinsic storage coefficient of the tissue; however, the argument was made for only for the acute-edema (EVP) case and no derivation was offered. Here, it is observed that the improved model, incorporating the intrinsic storage coefficient, yields a higher lower-estimate for the ion diffusion length in the case of acute edema; this shows that incorporating the parameter into the model may be of significance in clinical studies. In addition, in this manuscript, the technique is also employed to gauge the impact of hypertonic saline resuscitation (EVP-HS).

Section 5.2.1 overviews the basic premises leading to equation (5.6). Section 5.2.2 employs equation (5.6) to approximate the change in interstitial distance between the acute-edema (EVP) and resuscitated edema (EVP-HS) case. Section 5.2.3 builds on the results of Section 5.2.2 and discusses the support for the altered contractility capacity hypothesis.

5.2.1. Intestinal Motility In The Presence of Acute Edema, and Resuscitation

The motility of *luminal content* through the small bowel is enabled by contractions in the smooth muscle cells of the muscularis externa. Contractions are signaled by the diffusion of ions exiting a cell of Cajal or enteric neuron's synapse, crossing the interstitial space, and received by channels proximal to the smooth muscle cells. Excess interstitial fluid enlarges the interstitial region between cells, and increases the distance ions must traverse to reach their destination. Interstitial enlargement may cause a decrease in signaling capacity, and reduce contractile activity, due to the increased diffusion length. Clinical experiment suggests administration of 7.5% hypertonic saline

may restore contractile function to ileus-stricken tissue via a reduction in the volume-induced stress [23]. In this section we posit an additional argument in support of the primary clinical hypothesis; this argument is based on an approximation of the in-vivo increase in average synaptic diffusion length using the results of the computational clinical experiments. In a previous work [99] a similar argument was made for an early model which does not incorporate the intrinsic storage coefficient of the tissue; furthermore, the argument was made for only for the acute-edema (EVP) case and no derivation was offered. Here, it is observed that the proposed model, incorporating the intrinsic storage coefficient, yields a higher lower estimate for the ion diffusion length in the case of acute edema; this shows that incorporating the parameter into the model may be of significance in clinical studies. In addition, the technique is also employed to gauge the impact of hypertonic saline resuscitation, and a discussion of the diffusion length estimation methodology is put forth.

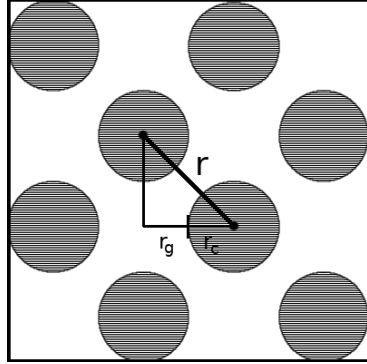


Figure 9: Smooth muscle distribution

The porosity of the muscle layer of the intestine is approximated by way of a simplified representative elementary volume. Following this the increase in average distance between smooth muscle cells post-edema is inferred; this yields equation (5.6) which expresses the deformed distance in terms of the relative bulk volume gain of the intestinal muscle layer. In section 5.2.2 equation (5.6) is applied to judge the relative difference between the control (CTRL), acute edema (EVP), and hypertonic-saline resuscitated acute edema (EVP-HS) computational test cases in order to estimate the impact of acute edema, and hypertonic saline resuscitation in-vivo. The average size of a smooth muscle cell is be-

tween $2\text{--}4\ \mu\text{m}$ wide, and $150\ \mu\text{m}$ long [49], with an average distance between neighboring smooth muscle cells in the range of $2\text{--}30\ \text{nm}$ [3, 25]. Approximating a smooth muscle cell as a cylinder with average radius between $2\text{--}4\ \mu\text{m}$ wide allows the construction of a simplified two-dimensional, cross-sectional, representative elementary volume with length $1\ \text{cm}$ and height equal to the radius of the cell plus the average gap size. The porosity, ϕ , in the representative elementary volume can then be estimated as $\phi \approx 22 - 24\%$. Smooth muscle cells express a range of phenotypes and a porosity estimate of $22\text{--}24\%$ is consistent with smooth muscle tissues whose purpose is almost exclusively contractile in nature; such porosities are typically between $15\% - 30\%$ [19].

In the context of edema the interstitium, e.g. the white area between the cells in figure 9, fills with additional fluid and pushes the cells, shaded gray, apart. The value of r , before and after edema can now be approximated. Using this approximation, an estimation of the horizontal gap length, e.g. the horizontal

distance between neighboring cells in the same row of figure 9, can then be made. The symbol \hat{r} is used to indicate the distance r post-edema. Letting r_c denote the cell radius, and r_g be half the horizontal, or vertical, gap length we have $r = \sqrt{2(r_c + r_g)^2}$. Following edema the change in base length, in figure 9, is given by $d(r_c + r_g) = dr_c + dr_g$. Assuming that the smooth muscle cell is impermeable to interstitial fluid gives $dr_c = 0$; thus the post-edema length, \hat{r} , is given by

$$\hat{r} = \sqrt{2(r_c + r_g + dr_g)^2} \quad (5.1)$$

Let V_s , V_p , and V_b denote the solid volume, pore volume, and bulk volume, respectively, of the muscle layer tissue. Then $V_b = V_s + V_p$ and $dV_b = dV_s + dV_p$; dividing the previous expression through by an increment in pressure, dP , and using the definition of compressibility [9, 60] for the bulk (C_b), solid (C_s), and pore phases (C_p) gives

$$-V_b C_b = V_p C_p - V_s C_s.$$

Assuming that the smooth muscle cell (solid phase) compressibility is much less than the tissue (bulk phase) compressibility gives $-V_b C_b \approx V_p C_p$. This can be expressed as $C_b \approx -\phi C_p$ where $\phi = V_p/V_b$ is the porosity of the tissue. Substituting $C_p = V_p^{-1}(dV_p/dP)$, $C_b = -V_b^{-1}(dV_b/dP)$, and the definition of the porosity in $C_b \approx -\phi C_p$ gives

$$\frac{dV_b}{dP} \approx \frac{dV_p}{dP},$$

from which the following relationship is obtained:

$$dV_b \approx dV_p. \quad (5.2)$$

Now $V_p = \phi V_b$ so that $dV_p = d\phi V_b + \phi dV_b$; *dividing* through by V_p , using the definition of the porosity ϕ , and (5.2) gives $d\phi \approx \phi(1 - \phi) dV_p/V_p$. If we instead divide by V_b , use the definition of ϕ , and (5.2) we have $d\phi \approx (1 - \phi) dV_b/V_b$. These results taken together yield

$$\frac{dV_p}{V_p} \approx \frac{1}{\phi} \frac{dV_b}{V_b}. \quad (5.3)$$

Supposing that the interstitial area between cells can be approximated by $V_p = Cr_g^2$, in two dimensions with $C > 0$, it follows that

$$\frac{dV_p}{V_p} = \frac{2dr_g}{r_g}. \quad (5.4)$$

Substitution of (5.4) into (5.3) gives

$$dr_g \approx \frac{r_g}{2\phi} \frac{dV_b}{V_b}. \quad (5.5)$$

Substitution of (5.5) into (5.1) yields an expression for \hat{r} in terms of the relative bulk volume change dV_b/V_b via

$$\hat{r} \approx \sqrt{2(r_c + r_g)^2 + 2(r_c + r_g)r_g y_b + \frac{1}{2}r_g^2 y_b^2} \quad (5.6)$$

where $y_b = \phi^{-1}(dV_b/V_b)$. The quantity dV_b/V_b has been measured for the computational model experiments, and the porosity estimate used is $\phi \approx 23\%$.

5.2.2. Estimating The Change In Interstitial Distance

Comp. Exp.	dV_b/V_b (%)	\hat{r} (nm)	\hat{r}_g (nm)
CTRL	0.1981	44.94 - 67.46	9.623 - 275.4
EVP	1.683	46.35 - 91.94	74.25 - 2227
EVP-HS	0.4985	45.23 - 73.08	22.70 - 670.1

Figure 10: Computed Relative Bulk Volume Gain and Gap Size Estimation

In order to establish a baseline for the estimation of the in-vivo effects of edema on intestinal motility, equation (5.6) is applied to the results of the control computational test (CTRL). This baseline is then used to deduce the relative increase for both the acute edema (EVP), and resuscitated edema (EVP-HS) case. Conclusions are inferred regarding the in-vivo intestinal motility from this relative change. Let \hat{r}_c , and \hat{r}_g denote the post-experimental cell radius and gap size, respectively, so that $\hat{r} = \sqrt{2(\hat{r}_c + \hat{r}_g)}$. Using the cell fluid-impermeability assumption ($\hat{r}_c = r_c$) average ranges for \hat{r}_g can be estimated for each computational case; results are shown in the table of figure 10. According to figure 10 the values of \hat{r}_g for the case of acute edema (EVP) are between 7.71 and 8.09 times larger with respect to the control case. For the hypertonic saline resuscitation (EVP-HS) case the average value of \hat{r}_g is between 2.36 and 2.43 times higher than those of the control.

5.2.3. Impact on Intestinal Motility

In section 4.4.1 it was discussed that a slightly lower oncotic blood pressure was found to produce computational results consistent with those of the clinical experiment, and that this could be due to trauma incurred by the surgical preparation procedure, etc. An increase in the interstitial distance between smooth muscle cells may be a primary factor in impaired contractility and intestinal motility due to the increased length that ions must diffuse. The purpose of this section is to compare approximations of the in-vivo interstitial distance for the EVP and EVP-HS cases; modulated primarily by \hat{r}_g . We conclude, based on the estimations, that hypertonic saline resuscitation could show promise for restoring intestinal motility.

To compare approximations for the EVP and EVP-HS interstitial distances, figure 10 is used to determine the relative values $\gamma_{EVP} = (\hat{r}_g^{EVP}/\hat{r}_g^{CTRL})$, and $\gamma_{EVP-HS} = (\hat{r}_g^{EVP-HS}/\hat{r}_g^{CTRL})$. It is assumed that under normal in-vivo conditions the interstitial distances, for EVP and EVP-HS, can also approximated

by these proportions. From figure 10 we see that γ_{EVP} takes on values between 7.716 and 8.09, likewise γ_{EVP-HS} lies between 2.359 and 2.433. As discussed in 5.2 the average in-vivo distance between smooth muscle cells for healthy, non-surgically treated specimens is between approximately 2 nm and 30 nm [3, 25].

Based on the assumption of relative proportions being preserved, the values for γ_{EVP} infer an average interstitial distance between 15.432 nm and 242.7 nm in the case of acute edema. Likewise, the values of γ_{EVP-HS} infer average interstitial distances between 4.718 nm and 72.99 nm for acute edema resuscitated by 7.5% hypertonic saline. The theoretical optimal length for the transmission of ion signals is postulated to lie within the range of 12-20 nm, with transmission distances beyond this distance being associated with reduced signaling capacity [80]. Thus, the administration of hypertonic saline in-vivo should lower the average interstitial distances between cells by a factor of approximately 3.3. Thus, it is reasonable to expect that resuscitation of acute edema with 7.5% hypertonic saline solution could realize a significant restoration of contractile function, and result in at least partially restoring intestinal motility. This result provides a new avenue of reasoning in agreement with the conclusion of the clinical hypothesis [23]; e.g. that of reduced motility in the case of acute edema, and the action of hypertonic saline in restoring contractile function.

5.3. Model Clarifications, and Further Experimental Suggestions

The proposed model of intestinal edema formation described in this manuscript combines the Starling-Landis-Drake-Laine clinical model of microvascular filtration and lymphatic exchange, with the equations of poroelasticity; thus coupling the clinical models of fluid exchange with the mechanical response of the intestinal tissue. In addition, the model incorporates a compensation for the overestimation of the Starling equation for high values of P_V , and incorporates a model of local tissue damage to the layered structure of the intestine. Due to the complexities of the model, there are several aspects that could be improved with additional experimental evidence.

First and foremost, additional clinical insight into constituents of the model would be highly beneficial. For instance, differences in the computational submucosal pressure averages versus reported submucosal transducer measurements may be further improved with additional parameter information. Some of this information, such as bulk Π_V before and after saline injection, may currently be measurable experimentally for the pre-and-post edema cases. Additional information on the combined permeability, κ , of the intestine and the constrained storage coefficients, c_1 , of the individual intestinal layers would also be welcome. These quantities have been measured in various ways for other tissue beds [31]. Measurements of the constrained storage coefficients, c_1 , may possibly be approximated by the use of ex-vivo clinical approaches such as the growth of appropriate tissue matrices on scaffolds [10] for use in subsequent measurements of mechanical properties. *Enhancements to the damage model, including the localization of μ and λ parameter changes based on soft-tissue injury studies, could provide further insight.*

Another aspect of the model that could be clarified by additional clinical experiment is the effect of high venous pressure on microvascular fluid flows; such effects include Starling overestimation, and the impacts of high venous pressure on the various parameters in the Starling model. A clarified statistical understanding of the relationship of the (K_f, σ) variation for venous pressures exceeding 15 mmHg (2000 Pa) seems to be lacking in the clinical literature. Moreover, a quantified understanding of the (K_f, σ) relationship to both P_V and the lymphatic pumping pressure, P_p , could improve the fluid model at high venous pressures.

It is known that a number of physiological ‘safety factors’ exist to ward against the formation of edema [47], but begin to break down near venous pressures exceeding $P_V \geq 15$ mmHg. A further complication in this regime is that experimental evidence suggests [1, 43, 51] flow may be driven more by local, rather than bulk, values of the oncotic pressures, Π_V and Π_I , and that the Starling equation, used with bulk tissue oncotic pressure values, may overestimate the microvascular fluid exchange as these values fluctuate locally. It is not presently clear if this dynamic implies that local micro-scale models, such as [1, 43], of the vascular endothelium are strictly necessary or if a homogenized correctional factor, endeavored here, can be reliably deduced from statistical approaches applied to experimental data that is robust with respect to a wide range of venous blood pressures.

In the current model, the basic approach of calibration of the (K_f, σ) pair, and its coupling to P_p , was done by selecting K_f and P_p from an early model [99] and employing the EVP experiment to find a suitable reduction in σ at the mean venous pressure of 20 mmHg (2666 Pa) observed in the clinical trials. The choices of K_f and P_p (see table 7) coincide with the known clinical heuristic observation [57, 81] that as P_V raises, K_f and P_p also increase, and that an increase in K_f implies a decrease in σ . In the clinical literature, however, the specifics of this relationship seem largely unexplored and the current understanding is limited to this qualitative description.

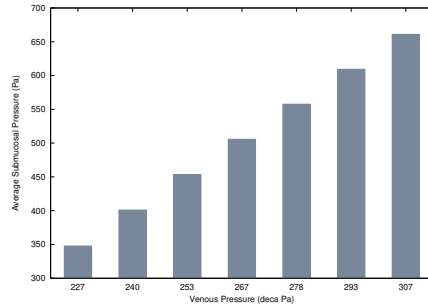


Figure 11: Admissible Experimental P_V (deca Pa) vs Computed Average Submucosal Pressure (Pa) EVP Experiment; $P_V \in [17, 23]$ mmHg, $[227, 307]$ dPa

A variation of P_V parameter test for the EVP computational case was conducted to test the voracity of the single-calibration approach for (K_f, σ) and P_p at median P_V . In the clinical experiment [23], measured values of P_V were reported to lie in the range of $[17, 23]$ mmHg (i.e. $[2266, 3066]$ Pa). The computational model was run using the fixed values of K_f and P_p , and calibrated σ , assessed for the $P_V = 20$ mmHg (2666 Pa) case, as mentioned

above. The computational results are shown in figure 11 with $P_V = 20$ mmHg (2666 Pa) corresponding to the middle bar and average computational submucosal pressures (in Pa) reported on the y-axis.

The sample standard deviation of the average submucosal pressures, over all computational experiments, is 0.84 mmHg (112 Pa) which higher than the experimentally reported value of 0.34 mmHg (45 Pa). However, if we consider the computational standard deviation for the experiments in a ‘nearby neighborhood’ of the mean value $P_V = 20$ mmHg (2666 Pa), used for calibration, such as $P_V \in [19, 21]$ mmHg (or [2533, 2800] Pa) then the standard deviation more closely matches the experimental standard deviation of 0.34 mmHg (45 Pa) at a value 0.39 mmHg (52 Pa). This indicates that using a single calibration around the mean vascular pressure may not be sufficient in accurately capturing the full dynamics of the (K_f, σ) and P_p relation across the large variation in P_V . We infer, then, that clinical experiments exploring this relation will be useful in constructing a more accurate computational model.

Despite the benefit that additional clinical understanding could offer the model, the predictive HS and EVP-HS computational experiments resulted in average submucosal pressures within the experimentally observed range. Based on the model observations, discussed in sections 4.4, 5.1, and 5.2 we agree with the clinical suggestion [23] that the hypertonic saline resuscitation technique offers promise in controlling the formation of acute edema in the presence of high venous pressure.

Nevertheless, the proposed computational model could be quite useful to clinicians. The computational average submucosal pressures for all cases are within experimental ranges, the final fluid content (EVP) is closely predicted, and the qualitative properties of the impact of HS administration in abetting acute edema are clearly observed. For these reasons, the proposed model may provide an effective qualitative benchmark for clinical research into the formation of edema in the intestine and for the a-priori judgment of the relative impact of various resuscitation fluids, in abetting edema, during a short-time (e.g. 5-60 min) window. Moreover, as further clinical understanding around the relationship between K_f , σ , and P_p , in the $P_V \geq 15$ mmHg regime, become well understood or as values for material parameters, such as c_1 and κ , within the intestine become available the model can be easily improved.

6. Conclusion

In this paper, we have described a numerical model of edema formation, based on the solution of Biot’s equations, and have demonstrated the potential suitability of the model in medical applications via the context of a clinical experiment in intestinal edema formation [23]. Physical parameters used in Biot’s model were selected from clinical literature for specific use in the intestine, or estimated using values from related organs where intestine-specific values were unavailable. The numerical approach, suitable for intestinal modeling, is a novel extension of a previous discretization proposed by the authors [77]; the model is implicit, and has previously been shown to abet spurious oscillations in

the pressure when used with dual penalty parameters [77]. These features confer some advantages over explicit approaches [99] such as a less restrictive time-step requirement, and the ability to model physically non-zero storage coefficients in the mass conservation equation (3.4).

In addition to the numerical and modeling advantages we have included a damage model for the tissue to account for the effects of excessive fluid pressures encountered in severe edema in addition to a capillary density in the fluid model approximating a physiological microvascular distribution [36, 99]. In addition, computational results suggest that the inclusion of the specific storage coefficient, unavailable in early models of intestinal edema [99], may be strongly advantageous for clinically related results.

Motivated by clinical experimental results [43] we proposed a simple extension of the fluid balance model (4.1) to account for the over-estimation of Starling forces in the presence of high venous blood pressure, and local oncotic pressure gradients, that may arise in the case of fluid resuscitation via 7.5% hypertonic saline. The over-estimation of Starling forces is an ongoing area of research in the clinical literature [1, 43, 51]. We have demonstrated that a calibrated, simplified model may be useful, from a computational standpoint, in edema models where more complex features of the microscale physiological features of vessel structures, such as the local characteristics of the endothelial glycocalyx, are not otherwise available.

Finally, the clinically observable model predictions (figure 6, submucosal plot) of the clinical voracity of hypertonic saline resuscitation for intestinal edema are in line with clinically observed results [23]. The proposed model is easily extensible as clinical experiments clarify additional relationships in the regime of high blood pressures, or as measurements of intestinal material properties are made available. Thus, the proposed method may show promise for clinicians modeling the effects of acute edema or fluid resuscitation agents in the planning of clinical experiments, or for various treatments.

7. Acknowledgement

The authors would like to acknowledge Drs. Marie Rognes, Alexandra Diem, and Cécile Daversin-Catty for the benefit of physiology related discussions and clinical literature suggestions. Moreover, the authors also acknowledge the contributions of the late Dr. Jennifer Young, whose work in pioneering early computational research models of intestinal edema formation continues as an inspiration to the community.

This research was conducted, in part, via the support of National Science Foundation grant NSF-DMS 1312391.

- [1] R.H. Adamson, J.F. Lenz, X. Zhang, G.N. Adamson, S. Weinbaum, and F.E. Curry. Oncotic pressures opposing filtration across non-fenestrated rat microvessels. *J Physiol*, 557(3):889–907, 2004.
- [2] E. Aifantis. On Barenblatt’s problem. *Lett. Appl. Engng. Sci.*, 18:857–867, 1980.

- [3] B. Alberts, A. Johnson, J. Lewis, M. Raff, K. Roberts, and P. Walter. *Molecular Biology of the Cell*. New York, Garland Science Press, 2 edition, 1994.
- [4] M. Bai, D. Elsworth, and J.-C. Roegiers. Multiporosity/Multipermeability Approach to the Simulation of Naturally Fractured Reservoirs. *Water Resources Research*, 6:1621–1633, 1993.
- [5] Satish Balay, Shrirang Abhyankar, Mark F. Adams, Jed Brown, Peter Brune, Kris Buschelman, Lisandro Dalcin, Victor Eijkhout, William D. Gropp, Dinesh Kaushik, Matthew G. Knepley, Dave A. May, Lois Curfman McInnes, Karl Rupp, Patrick Sanan, Barry F. Smith, Stefano Zampini, Hong Zhang, and Hong Zhang. PETSc users manual. Technical Report ANL-95/11 - Revision 3.8, Argonne National Laboratory, 2017.
- [6] Satish Balay, Shrirang Abhyankar, Mark F. Adams, Jed Brown, Peter Brune, Kris Buschelman, Lisandro Dalcin, Victor Eijkhout, William D. Gropp, Dinesh Kaushik, Matthew G. Knepley, Dave A. May, Lois Curfman McInnes, Karl Rupp, Barry F. Smith, Stefano Zampini, Hong Zhang, and Hong Zhang. PETSc Web page. <http://www.mcs.anl.gov/petsc>, 2017.
- [7] Satish Balay, William D. Gropp, Lois Curfman McInnes, and Barry F. Smith. Efficient management of parallelism in object oriented numerical software libraries. In E. Arge, A. M. Bruaset, and H. P. Langtangen, editors, *Modern Software Tools in Scientific Computing*, pages 163–202. Birkhäuser Press, 1997.
- [8] G.I. Barenblatt, Iu.P. Zheltov, and I.N. Kochina. Basic concepts in the theory of seepage of homogeneous liquids in fissured rocks (strata). *PMM*, 24(5):852–864, 1960.
- [9] J. Bear and Y. Bachmat. *Introduction to modeling of transport phenomena in porous media*. Kluwer Academic Press, 1990.
- [10] M.W. Beatty, A.K. Ojha, J.L. Cook, L.R. Alberts, G.K. Mahanna, L.R. Iwasaki, and J.C. Nickel. Small intestinal submucosa versus salt-extracted polyglycolic acid-poly-l-lactic acid: a comparison of neocartilage formed in two scaffold materials. *Tissue Eng.*, 8:955–968, 2002.
- [11] D. Beskos and E. Aifantis. On the theory of consolidation with double porosity – ii. *Int. J. Engng. Sci.*, 24:1697–1716, 1986.
- [12] M. Biot. General theory of three-dimensional consolidation. *J. Appl. Phys.*, 12:155–164, 1941.
- [13] M. Biot. Theory of elasticity and consolidation for a porous anisotropic media. *J. Appl. Phys.*, 26(2):182–185, 1955.

- [14] M. Biot. Nonlinear and semilinear rheology of porous solids. *J. Geophy. Res.*, 73:4924–4937, 1973.
- [15] M. Biot and D. Willis. The elastic coefficients of the theory of consolidation. *J. Appl. Mech.*, 24:594–601, 1957.
- [16] J. Böck, B. Barker, A. Clinton, B. Wilson, and F. Lewish. Post-traumatic Changes in, and Effect of Colloid Osmotic Pressure on the Distribution of Body Water. *Ann. Surg.*, 210(3):395–405, 1989.
- [17] J.R. Booker and J.C. Small. An investigation of the stability of numerical solutions of biot’s equations of consolidation. *Int J. Solids Structures*, 2011:907–917, 1975.
- [18] B. Brenner, I. Ueki, and T. Daugharty. On estimating colloid osmotic pressure in pre- and postglomerular plasma in the rat. *Kidney International*, 2:51–53, 1972.
- [19] G.R. Campbell and J.H. Campbell. Development of the Vessel Wall: Overview. In S. Schwartz and R. Mecham, editors, *The Vascular Smooth Muscle Cell*, pages 1–15. Academic Press, 1995.
- [20] C. Chapple, B. Bowen, R. Reed, S. Xie, and J. Bert. A model of human microvascular exchange: parameter estimation based on normals and nephrotics. *Comput. Methods Programs Biomed.*, 41:33–54, 1993.
- [21] D. Chou, J.C. Vardakis, L. Guo, B.J. Tully, and Y. Ventikos. A fully dynamic multi-compartmental poroelastic system: application to aqueductal stenosis. *J. Biomech.*, 49(11):2306–2312, 2016.
- [22] A.M. Collinsworth, S. Zhang, W.E. Kraus, and G.A. Truskey. Apparent elastic modulus of hysteresis of skeletal muscle cells throughout differentiation. *Am. J. Physiol. Cell Physiol.*, 283:C1219–1227, 2002.
- [23] C.S. Cox, R. Radhakrishnan, L. Vilarubia, H. Xue, K. Uray, B. Gill, R. Stewart, and G. Laine. Hypertonic saline modulation of intestinal tissue stress and fluid balances. *Shock*, 29:598–602, 2008.
- [24] J. De La Puente, M. Dumbser, M. Käser, and H. Igel. Discontinuous Galerkin methods for wave propagation in poroelastic media. *Geophysics*, 73(5):T77–T79, 2008.
- [25] C.E. Devine, F.O. Simpson, and W.S. Bertraud. Freeze-etch studies on the innervation of mesenteric arteries and vas deferens. *J. Cell. Sci.*, 9:411–425, 1971.
- [26] M. Doblare and J. Merodio. *Biomechanics*. EOLSS Publications, 2015.
- [27] R.M. Dongaonkar, G.A. Laine, R.H. Stewart, and C.M. Quick. Balance point characterization of interstitial fluid volume regulation. *Ann. J. Physiol. Regul. Integr. Comp. Physiol.*, 297:R6–R16, 2009.

- [28] R.M. Dongaonkar, G.A. Laine, R.H. Stewart, and C.M. Quick. Evaluation of gravimetric techniques to estimate the microvascular filtration coefficient. *Ann. J. Physiol. Regul. Integr. Comp. Physiol.*, 300:R1426–R1436, 2011.
- [29] R.M. Dongaonkar, C.M. Quick, R.H. Stewart, R.E. Drake, C.S. Cox, and G.A. Laine. Edemagenic gain and interstitial fluid volume regulation. *J. Physiol. Regul. Integr. Comp. Physiol.*, 294:651–659, 2008.
- [30] D. Drobin and R. Hahn. Kinetics of Isotonic and Hypertonic Plasma Volume Expanders. *Anesthesiology*, 96:1371–1380, 2002.
- [31] J. Durand, W. Durand-Arczynska, and P. Haab. Volume flow, hydraulic conductivity, and electrical properties across bovine tracheal epithelium in vitro: effect of histamine. *European J. Physiology*, 395:40–45, 1981.
- [32] B. Fisher, D. Thomas, and B. Peterson. Hypertonic saline lowers raised intracranial pressure in children after head trauma. *J. Neurosurg. Anestiol.*, 4:4–10, 1992.
- [33] J. Gamble, L. Smaje, and P. Spencer. Filtration coefficient and osmotic reflection coefficient to albumin in rabbit submandibular gland capillaries. *J. Physiology*, 398:15–32, 1988.
- [34] C. Geuzaine and J.-F. Remacle. Gmsh: a three-dimensional finite element mesh generator with built-in pre-and post-processing facilities. *Int. J. Num. Meth. Engrg.*, 79(11):1309–1331, 2009.
- [35] H. Golab, T. Scochy, P. de Jong, J. Kissler, J. Takkenberg, and J. Bogers. Relevance of colloid oncotic pressure regulation during neonatal and infant cardiopulmonary bypass: a prospective randomized study. *European J. Cardio-thoracic Surgery*, 39:886–891, 2011.
- [36] D.N. Granger and J. Barrowman. Gastrointestinal and liver edema. In N.C. Staub and A.E. Taylor, editors, *Edema*, pages 615–656. Raven Press, New York, 1984.
- [37] B. Griffin and C. O’Driscoll. Models of the small intestine. In C. Ehrhardt and K.-J. Kim, editors, *Drug Absorption Studies: In Situ, In Vitro and In Silico Models*, pages 34–76. Springer US, Boston, MA, 2008.
- [38] A.C. Guyton. Interrelationships among interstitial fluid volume, interstitial fluid pressure, interstitial fluid protein concentration and lymph flow. In R.K. Reed, N.G. McHale, J.L. Bert, C.P. Winlove, and G.A. Laine, editors, *Interstitium, Connective Tissue and Lymphatics: Proceedings of the XXXII Congress of the International Union of Physiological Sciences*, pages 167–180, London, 1995. Portland Press.
- [39] A.C. Guyton and J.E. Hall. *Textbook of Medical Physiology*. Elseiver Saunders, 11 edition, 2006.

- [40] C.C. Gyenge, B.D. Bowen, R.K. Reed, and J.L. Bert. Transport of fluid and solutes in the body I: formulation of a mathematical model. *Ann. J. Physiol. Heart Circ. Physiol.*, 277:1215–1227, 1999.
- [41] MPM (auth.) Hans Gregersen MD, DrMSci. *Biomechanics of the Gastrointestinal Tract: New Perspectives in Motility Research and Diagnostics*. Springer-Verlag, London, 2003.
- [42] P. Hansbro and M.G. Larson. Discontinuous Galerkin method for incompressible and nearly compressible elasticity by Niche’s method. *Computer Meth. for Appl. Mech. Engrg.*, 191:1895–1908, 2002.
- [43] X Hu, R.H. Adamson, B. Liu, F.E. Curry, and S. Weinbaum. Starling forces that oppose filtration after tissue oncotic pressure is increased. *Am J Physiol Heart Circ Physiol*, 279:H1724–H1736, 2000.
- [44] F.R. Johnson. The digestive system. In G.J. Romanes, editor, *Edema*, pages 411–489. Oxford University Press, Oxford, 1981.
- [45] M. Khaled, D. Beskos, and E. Aifantis. On the theory of consolidation with double porosity – iii A finite element formulation. *Int. J. Num. and Analy. Meth. Geomech.*, 8:101–123, 1984.
- [46] M.P. Kinsky, S.M. Milner, B. Button, M.A. Dubick, and G.C. Kramer. Resuscitation of severe thermal injury with hypertonic saline dextran: effects on peripheral and visceral edema in sheep. *J. Trauma*, 49:844–853, 2000.
- [47] P. Kvietz. *The Gastrointestinal Circulation*. Morgan & Claypool Life Sciences, London Health Science Center, 2010.
- [48] E.M. Landis. Micro-injection studies of capillary permeability II. the relation between capillary pressure and the rate at which fluid passes through the walls of single capillaries. *Am. J. Physiol.*, 82:217–238, 1927.
- [49] B.P. Lane. Alterations in the cytologic detail of intestinal smooth muscle cells in various stages of contraction. *J. Cell. Biol.*, 27:199–213, 1965.
- [50] J. Lee, K.-A. Mardal, and R. Winther. Parameter-robust discretization and preconditioning of Biot’s consolidation model. *SIAM J. on Sci. Comput.*, 39(1):A1–A24, 2017.
- [51] R.L. Levick. Revision of the Starling principle: new views of tissue fluid balance. *J Physiol*, 55:704, 2004.
- [52] Xiaoye S. Li. An overview of SuperLU: Algorithms, implementation, and user interface. *ACM Transactions on Mathematical Software*, 31(3):302–325, September 2005.
- [53] Xiaoye S. Li and Meiyue Shao. A supernodal approach to incomplete LU factorization with partial pivoting. *ACM Trans. Mathematical Software*, 37(4), 2010.

- [54] X.S. Li, J.W. Demmel, J.R. Gilbert, iL. Grigori, M. Shao, and I. Yamazaki. SuperLU Users' Guide. Technical Report LBNL-44289, Lawrence Berkeley National Laboratory, September 1999. <http://crd.lbl.gov/~xiaoye/SuperLU/>. Last update: August 2011.
- [55] A. Linninger, K. Tangen, C.-Y. Hsu, and D. Frim. Cerebrospinal Fluid Mechanics and Its Coupling to Cerebrovascular Dynamics. *Ann. Rev. of Fluid Mech.*, 48(1):219–257, 2016.
- [56] C. Lucas, D. Benishek, and A. Ledgerwood. Reduced Oncotic Pressure After Shock. *Arch. Surg.*, 117:675–679, 1982.
- [57] M. Maron, Z. Fu, O. Mathieu-Costello, and J. West. Effect of high transcapillary pressures on capillary ultrastructure and permeability coefficients in dog lung. *J Appl Physiol*, 90:639–648, 2001.
- [58] M. Mattay. Resolution of Pulmonary Edema. *Am. J. Respir. Crit. Care Med.*, 189(11):1301–1308, 2014.
- [59] M.C. Mazzoni, P. Borgstrom, K.E. Arfors, and M. Intaglietta. Dynamic fluid redistribution in hyperosmotic resuscitation of hypovolemic hemorrhage. *Ann. J. Physiol. Heart Circ. Physiol.*, 255:H629–H637, 1988.
- [60] A. Merxhani. An introduction to linear poroelasticity. *ArXiv e-prints*, July 2016.
- [61] M. Miga, K. Paulsen, and F. Kennedy. Von Neumann stability analysis of Biot's general two-dimensional theory of consolidation. *Int. J. Numer. Meth. Engng.*, 43:955–974, 1998.
- [62] M. Miller, J. McDole, and R. Newberry. Microanatomy of the intestinal lymphatic system. *Ann. N.Y. Acad. Sci.*, 1207:E21–E28, 2010.
- [63] M. Mokhtarudin and S. Payne. The study of the function of AQP4 in cerebral ischaemia-reperfusion injury using poroelastic theory. *Int. J. Numer. Meth. Biomed. Engng.*, 33(1):1–14, 2017.
- [64] S.D. Moore-Olufemi, J. Padalecki, S.E. Olufemi, H. Xue, D.H. Oliver, R.S. Radhakrishnan, S.J. Allen, F.A. Moore, R. Stewart, G.A. Laine, and C.S. Cox. Intestinal edema: effect of enteral feeding on motility and gene expression. *J. Surg. Res.*, 155:283–292, 2009.
- [65] S.D. Moore-Olufemi, H. Xue, S.J. Allen, F.A. Moore, R.H. Stewart, G.A. Laine, and C.S. Cox. Inhibition of intestinal transit by resuscitation induced gut edema in is reversed by l-nil. *J. Surg. Res.*, 129:1–5, 2005.
- [66] S.D. Moore-Olufemi, H. Xue, B.O. Attuwaybi, U. Fischer, Y. Harari, D.H. Oliver, N. Weisbrodt, S.J. Allen, F.A. Moore, and R. Stewart. Resuscitation-induced gut edema and intestinal dysfunction. *J. Trauma*, 58:264–270, 2005.

- [67] T. Nagashima, T. Shirakuni, and S. Rapoport. A Two-dimensional, Finite Element Analysis of Vasogenic Brain Edema. *Neurol. Med. Chir. (Tokyo)*, 30:1–9, 1990.
- [68] G. Öhqvist, G. Settergren, K. Bergström, and S. Lundberg. Plasma colloid osmotic pressure during open-heart surgery using non-colloid or colloid priming solution in the extracorporeal circuit. *Scand. J. Thor. Cardiovasc. Surg.*, 15:251–255, 1980.
- [69] J.R. Pappenheimer and A. Soto-Rivera. Effective osmotic pressure of the plasma proteins and other quantities associated with the capillary circulation in the hindlimbs of cats and dogs. *Am. J. Physiol.*, 152:471–491, 1948.
- [70] P. Phillips and M. Wheeler. Overcoming the problem of locking in linear elasticity and poroelasticity: a heuristic approach. *Comput. Geosci.*, (13):5–12, 2009.
- [71] R. Radhakrishnan, H. Xue, N. Weisbrodt, F.A. Moore, S.J. Allen, G.A. Laine, and C.S. Cox. Resuscitation-induced intestinal edema decreases the stiffness and residual stress of the intestine. *Shock*, 24:165–170, 2005.
- [72] R.S. Radhakrishnan, H. Xue, N.W. Weisbrodt, F.A. Moore, S.J. Allen, G.A. Laine, and C.S. Cox. Hypertonic saline prevents hydrostatically induced intestinal edema and ileus. *Crit. Care. Med.*, 34:1713–1718, 2006.
- [73] S. Rapoport. A Mathematical Model for Vasogenic Brain Edema. *J. theor. Biol.*, 74:439–467, 1978.
- [74] R. Reed and K. Aukland. Transcapillary fluid balance in immature rats. interstitial fluid pressure, serum and interstitial protein concentration, and colloid osmotic pressure. *Microvascular Research*, 14(1):37 – 43, 1977.
- [75] R.K. Reed. Interstitial fluid pressure. In R.K. Reed, N.G. McHale, J.L. Bert, C.P. Winlove, and G.A. Laine, editors, *Interstitium, Connective Tissue and Lymphatics: Proceedings of the XXXII Congress of the International Union of Physiological Sciences*, pages 85–100, London, 1995. Portland Press.
- [76] B.M. Rivière. *Discontinuous Galerkin Methods for Solving Elliptic and Parabolic Equations: Theory and Implementation*. SIAM, Philadelphia, 2005.
- [77] B.M. Rivière, J. Tan, and T. Thompson. Error Analysis Of Primal Discontinuous Galerkin Methods For A Mixed Formulation Of The Biot Equations. *Comp. and Math. with Appl.*, 73(4):666–683, 2017.
- [78] C. Rodrigo, Gaspar F.J., X. Hu, and L.T. Zikatanov. Stability and monotonicity for some discretizations of the Biot’s consolidation model. *Comput. Methods Appl. Mech. Engrg.*, (298):183–204, 2016.

- [79] M. Sanders, S. Ward, and S.-D. Koh. Interstitial Cells: Regulators Of Smooth Muscle Function. *Physiol. Rev.*, 94:859–907, 2014. doi:10.1152/physrev.00037.2013.
- [80] L.P. Savtchenko and D.A. Rusakov. The optimal height of the synaptic cleft. *PNAS*, 104:1823–1828, 2007.
- [81] J. Scallen, V. Huxley, and R. Korthuis. *Capillary Fluid Exchange: Regulation, Functions, and Pathology*. Morgan and Claypool Life Sciences, 2010.
- [82] S. Shah, K. Uray, R. Stewart, G. Laine, and C. Cox. Resuscitation-Induced Intestinal Edema and Related Dysfunction: State of the Science. *J. Surg. Res.*, 166:120–130, 2011.
- [83] R.E. Showalter. Diffusion in Poro-Elastic Media. *J. of Math. Analysis and App.*, 251:310–340, 2000.
- [84] D. Taylor, J. Bert, and B. Bown. A mathematical model of interstitial transport: I. theory. *Microvasc. Res.*, 39(3):253–278, 1990.
- [85] K. Terzaghi. *Theoretical Soil Mechanics*. Wiley, 1943.
- [86] B. Tully and Y. Ventikos. Coupling poroelasticity and cfd for cerebrospinal fluid hydrodynamics. *IEEE Trans. Biomed. Eng.*, 56:1644–1651, 2009.
- [87] B. Tully and Y. Ventikos. Cerebral water transport using multiple-network poroelastic theory: application to normal pressure hydrocephalus. *J. Fluid Mech.*, 667:188–215, 2011.
- [88] N. Unno, M. Nishiyama, M. Suzuki, H. Tanaka, N Yamamoto, D. Sagara, Y. Mano, and H. Konno. A novel method of measuring human lymphatic pumping using indocyanine green fluorescene lymphography. *J. Vasc. Surg.*, 52:946–952, 2010.
- [89] R. Vaishnav and J. Vossoughi. RESIDUAL STRESS AND STRAIN IN AORTIC SEGMENTS. *J. Biomechanics*, 20(3):235–239, 1987.
- [90] J.C. Vardakis, D. Chou, B. Tully, C. Hung, T. Lee, P.-H. Tsui, and Y. Ventikos. Investigating cerebral oedema using poroelasticity. *Med. Eng. and Phy.*, 38:48–57, 2016.
- [91] J.C. Vardakis, B.J. Tully, and Y. Ventikos. Multicompartmental poroelasticity as a platform for the integrative modeling of water transport in the brain. In G.A. Holzapfel and E. Kuhl, editors, *Computer Models in Biomechanics*, pages 305–316. Springer, New York, 2013.
- [92] T. Vilz, B. Stoffels, C. Strassburg, H. Schild, and J. Kalff. Ileus in Adults. *Dtsch. Arztebl. Int.*, 114:508–518, 2017.

- [93] B.A. Waaler and P. Aarseth. Interstitial fluid and transcapillary fluid balance in the lung. *Ciba Found Symp.*, 38:65–76, 1976.
- [94] F. Wiener, W. Carson, V.K. Puri, and M.H. Weil. Mathematical model to study fluid and protein transfer in pulmonary edema in man. *Crit. Care Med.*, 11:132–141, 1983.
- [95] T.P. Wihler. Locking-free DGFEM for elasticity problems in polygons. Eidgenössische Technische Hochschule, 2002. Technical Research Report. Seminar für Angewandte Mathematik.
- [96] H. Wiig and M. Swartz. Interstitial Fluid And Lymph Formation And Transport: Physiological Regulation And Roles In Inflammation And Cancer. *Physiol. Rev.*, 92:1005–1060, 2012.
- [97] R.K. Wilson and E. Aifantis. On the theory of consolidation with double porosity. *Int. J. Engng. Sci.*, 20:1009–1035, 1982.
- [98] J. Young and B. Rivière. The Development of a Computational, Poroelastic Model of Intestinal Edema. VUB, Brussels, Belgium, Sept, 21-23 2011. Proceedings of the ECCOMAS Thematic International Conference on Simulation and Modeling of Biological Flows (SIMBIO 2011).
- [99] J. Young, B. Rivière, C. Cox, and K. Uray. A mathematical model of intestinal edema formation. *Math. Medic. and Bio.*, 30(4):1189–1210, 2012.